A Lagrangian description of transport associated with a fronteddy interaction

A Lagrangian description of transport associated with a Front-Eddy interaction: application to data from the North-Western Mediterranean Sea

Michał Branicki[1], Ana M. Mancho[2], Stephen Wiggins[1]

[1] School of Mathematics, University of Bristol, Bristol, United Kingdom

[2] Instituto de Ciencias Matemáticas, CSIC-UAM-UC3M-UCM, Madrid, Spain

September 20, 2010

Abstract

We discuss the Lagrangian transport in a time-dependent oceanic system involving a Lagrangian barrier associated with a salinity front which interacts intermittently with a set of Lagrangian eddies - 'leaky' coherent structures that entrain and detrain fluid as they move. A theoretical framework, rooted in the dynamical systems theory, is developed in order to describe and analyse this situation. We show that such an analysis can be successfully applied to a realistic ocean model. Here, we use the output of the numerical ocean model DieCAST [12, 16] studied earlier in [30] where a Lagrangian barrier associated with North Balearic Front in the Northwestern Mediterranean Sea was identified. The numerical model provides an Eulerian view of the flow and we employ the dynamical systems approach to identify relevant hyperbolic trajectories and their stable and unstable manifolds. These manifolds are used to understand the Lagrangian geometry of the evolving front-eddy system. Transport in this system is effected by the turnstile mechanism whose spatio-temporal geometry reveals intermittent pathways along which transport occurs. Particular attention is paid to the 'Lagrangian' interactions between the front and the eddies, and to transport implications associated with the transition between the one-eddy and two-eddy situation. The analysis of this 'Lagrangian' transition is aided by a local kinematic model that provides insight into the nature of the change in hyperbolic trajectories and their stable and unstable manifolds associated with the 'birth' and 'death' of leaky Lagrangian eddies.

1 Introduction

Advances in observational methods and in computational resources have revealed a variety of flow structures in the ocean, such as jets, fronts, and eddies, that evolve in a 'coherent' fashion despite their highly convoluted instantaneous geometry. Recent observations and experiments indicate that these structures significantly influence transport characteristics of the geophysical-scale flows (see, for example [43]). The global, geometrical framework of nonlinear dynamical systems theory, which helps uncover the role that localised structures

play in influencing the motions of collections of trajectories in space and time, has proven to be useful for analysing transport issues in fluid flows. The application of this mathematical approach to realistic geophysical flows has required the development of new concepts in dynamical systems theory, resulting in the notion of 'finite-time dynamical systems'. Recent reviews of this framework in the context of oceanographic flows can be found in [45, 32, 41], and we briefly discuss the relevant issues at the beginning of §3.

The zonally propagating jet is one example of a geophysical flow structure that has been the subject of extensive analysis within the geometrical framework of dynamical systems. Beginning with the work of Bower [4], a variety of kinematic models of jets have been considered ([42, 13, 15, 34, 5]) which paved the way for the analysis of transport in dynamically consistent models of jets ([39, 46, 47]). The insight and mathematical ideas developed in the course of these studies were then used to develop a deeper understanding of the Gulf Stream from observational data by Lozier et al. [26]. This progression of work on transport in zonally propagating jets illustrates the power and flexibility of the dynamical systems approach. Whether the flow is realised as a kinematic model, dynamical model, or a model obtained from observations, the abstract approach of dynamical systems theory is the same in each case, regardless of the specific form of the velocity field under consideration. In [30] this approach was used to study transport associated with a front in the North-Western Mediterranean Sea using a high resolution numerical ocean model, DieCAST, developed in [11, 12, 16]. It was shown there that the dynamical systems approach could be used to give a geometrical characterization of the front in a manner that allowed both qualitative and quantitative analyses of transport properties. In particular, it was shown that the location of the front could be identified as a "Lagrangian barrier" across which transport is weak. Moreover, transport to, across, and away from the front occurred by a complex spatio-temporal route of filaments that could be described and quantified with the ideas of lobe dynamics.

In [30], where the Lagrangian front was the only analysed structure, the authors pointed out that transport across the front could be affected by nearby eddies. In this work we continue the analysis of Lagrangian transport in the North-Western Mediterranean Sea by considering the situation where the front interacts with one, or two, oceanic eddies. Such a flow configuration opens up a wealth of new spatio-temporal transport pathways in the considered flow which we identify and explain using the framework developed here.

There is an important concept that we address and develop further in this paper. While the Lagrangian description of jets and fronts in the context of dynamical systems theory is well established, a Lagrangian description of an eddy is more elusive. This conceptual problem seems to originate from the fact that while the traditional understanding and view of an eddy is Eulerian in nature, the transport issues associated with such structures are inherently Lagrangian. Eulerian eddies are often identified from by tracking the evolution of closed contours vorticity, contours of the see surface height, or using the Okubo-Weiss criterion [38]. However, a key feature transpiring from observations is that eddies are 'leaky' coherent structures that entrain and detrain fluid as they evolve. Hence, it seems that a Lagrangian eddy should not be defined by the fluid that it contains. We will provide such a definition in this paper that is appropriate for our needs. We remark that the 'Lagrangian description of an eddy' is a topic of current importance as a result of recently obtained data sets showing that eddies play a very important role in transport processes in the ocean ([7]).

In complex time-dependent flows one can often observe the appearance and disappearance of Eulerian eddies. As will be shown in the following sections, these events are, in some cases, signatures of Lagrangian transitions in the flow which have important consequences on transport characteristics, opening up new transport pathways. However, there is no general relationship between the Eulerian and Lagrangian flow transitions. Consequently, it is impossible to determine purely from the Eulerian observations whether, for example, a

'birth' of an Eulerian eddy was accompanied by a change in the underlying Lagrangian flow structure. Our work not only develops the theoretical framework to describe and analyse this situation, but it also shows that it can be applied to a realistic ocean model.

The structure of the paper is as follows. In §2 we describe the relevant Eulerian flow features which lead to identification of the front-eddy system in the velocity field generated by a realistic, high resolution model of the Mediterranean Sea. In §3 we introduce the dynamical systems tools required to describe the geometry and transport in the front-eddy system. It is also in this section where we discuss the Lagrangian description of an eddy. In §4 we use the tools of §3 to describe transport in the flow generated by the numerical model introduced in §2. The analysis is carried out by first identifying two distinct Lagrangian flow configurations, referred to as Scenario I and II, which intermittently dominate the flow structure. We then identify transport pathways associated with each of these configurations separately and use the insight provided by such analysis to understand how transitions between these Lagrangian configurations can occur. The Lagrangian geometry associated with these intermittent transitions is discussed in more detail in §4.3. Finally, §5 presents the conclusions as well as describes some outstanding issues and directions for future work.

2 The Ocean Circulation Model and the Eulerian Structures of Interest

The details of the numerical model, sufficient for our purposes, can be found in [30], but we provide a brief summary of features that may be of immediate interest for this work.

The velocity field that we study is obtained from an ocean model, DieCAST [11], adapted to the Mediterranean Sea [12, 16]. The model uses the 3D primitive equations and is discretised with a fourth-order collocated control volume method. The model is initialized at a state of rest and the spin-up phase of integration is carried out for 16 years. Each year is considered to have 12 months of 30 days length each (i.e. 360 days). Details of boundary conditions, physical parameters such as horizontal and vertical viscosity and diffusivity, and the various types of forcing can be found in the above references.

The horizontal resolution is the same in both the longitudinal (ϕ) and latitudinal (λ) directions, with $\Delta\phi = (1/8)$ of degree and $\Delta\lambda = \Delta\phi \cos\lambda$ thus making square horizontal control volume boundaries. The vertical resolution is variable, with 30 control volume layers. The thickness of control volumes in the top layer is 10.3 m and they are smoothly increased up to the deepest bottom control volume face at 2750 m.

We focus on velocity fields obtained at the second layer which has its center at a depth of 15.93 m. This is representative of the surface circulation and is not as directly driven by wind as the top layer. Figure 1 shows the velocity field at day 679 (the 19th day of the eleventh month – November – of the second year). The instantaneous stagnation points (ISPs; see Appendix A.1) are displayed: the hyperbolic ISPs (i.e. saddle points in the linear, frozen-time approximation) are denoted with a cross and the elliptic ISPs (i.e. stable points in the linear (frozen-time) approximation) are denoted with a gray dot. The area of interest is located in the Western Mediterranean Sea and the Eulerian current studied in [30] is highlighted with the dark straight line. At the Eastern end of the dark straight line we show a dark circle surrounding an elliptic ISP, which we recognize as the Eulerian signature of an eddy.

Figure 2 shows the velocity field at day 683 (the 23rd day of the eleventh month – November – of the second year). We illustrate the same Eulerian features as in 1, but we also highlight a smaller (Eulerian) eddy (marked with a small dark circle) that has appeared after a saddle node bifurcation of ISPs at day 680 (the signature that the saddle-node bifurcation of ISPs occurred is the additional pair of ISPs, one saddle and one elliptic, at the Eastern

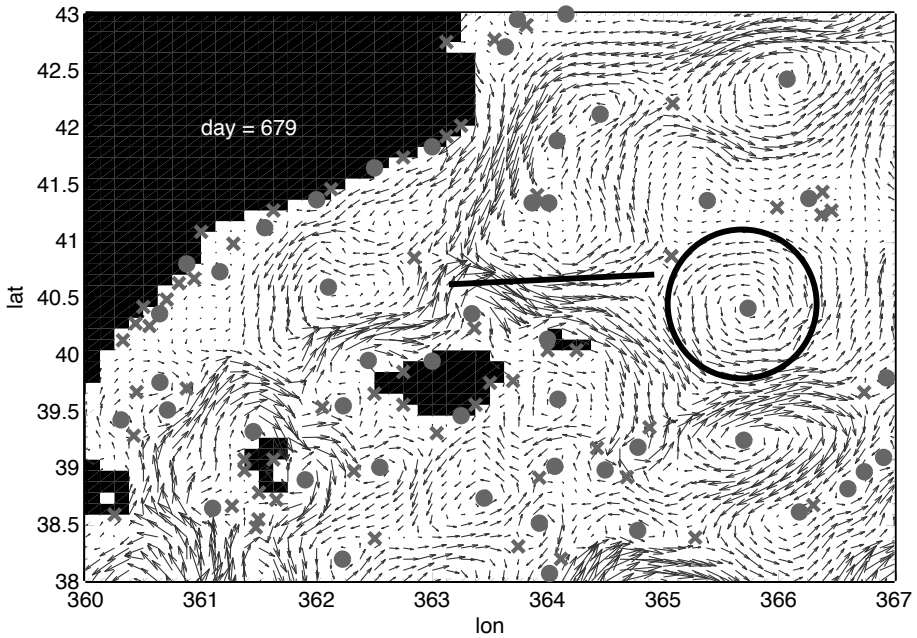

Figure 1: **DieCAST model, NW Mediterranean.** The velocity field at day 679 showing the Eulerian current (denoted by the dark line) studied in [30] as well as an Eulerian eddy at the eastern end of the current. This situation is often associated with a Lagrangian flow structure referred to hereafter as Scenario I. In this figure the dark regions represent land. The large dark region of the upper left hand corner is Spain, the large island in the middle is Majorca, the small island to the right of Majorca is Menorca, and the island to the left of Majorca is Ibiza.

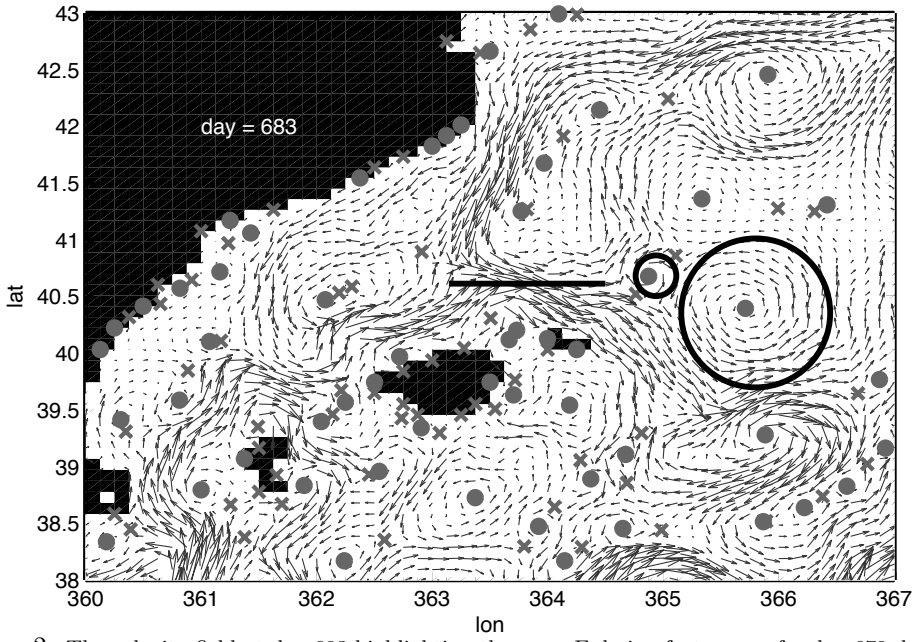

Figure 2: The velocity field at day 683 highlighting the same Eulerian features as for day 679, but with an additional (small) Eulerian eddy at the eastern end of the current resulting from the creation a new elliptic ISP in a saddle-node bifurcation at day 680. This situation is often associated with existence a Lagrangian structure referred to later as Scenario II.

end of the straight line).

The velocity field has small vertical components, so therefore this is not strictly a two dimensional flow. It is important to bear in mind that the vertical velocity is not a primary variable in most ocean models (including DieCAST) and it is inferred instead from some variant of the continuity equation. Vertical velocities in the top layers in the DieCAST model are of the order of 10^{-5} m/s, and it is argued in [30] that, as a rule of thumb, we can consider that trajectories preserve two dimensionality during time intervals of about 20 days. We discuss a much more general justification of 2D analysis in stratified 3D flows in Appendix B. Our arguments do not rely on smallness of the vertical velocities. Instead, we argue that the 2D Lagrangian techniques can be used to study transport in a layer whose thickness depends on the ratio between average horizontal velocities in the layer to the average vertical shear of the horizontal velocity components. The key fact is that within such a layer one may analyse the geometry of a time-dependent transport barrier which maintains its (approximately) invariant properties in the horizontal directions while allowing some trajectories to leave or enter it from layers below or above it (see figure 20).

Our goal is to understand the Lagrangian transport features associated with scenarios I and II, as well as how they change in the transition between these two scenarios. In order to do this, we will need to develop a Lagrangian characterization of these Eulerian features, and we will develop the tools and concepts for doing this in the next section. However, it is important to realize that our Lagrangian analysis is guided by the Eulerian features of the data set.

3 Dynamical Systems perspective of Lagrangian transport

In this section we recall the basic tools from dynamical systems theory that we will use to analyse Lagrangian transport of the front-eddy system. Following many earlier works using the dynamical systems approach for analyzing Lagrangian transport in unsteady flows (see references in §1), the notion of hyperbolicity is central to our analysis and it provides the means for characterizing trajectories in time-dependent flows which behave like "moving saddle points". These hyperbolic trajectories have stable and unstable invariant manifolds[1] (see Appendix A.3) which, similarly to the separatrix manifolds of saddle points in steady flows, can be used to identify boundaries between distinct regions in the flow domain. In particular, we will use the stable and unstable manifolds of the so-called Distinguished Hyperbolic Trajectories (DHTs) (see Appendix A.2), to construct a Lagrangian front, i.e. an elongated transport barrier which strongly inhibits transport across it (here we follow [30]), and a Lagrangian eddy (or eddies) characterised by an area of predominantly recirculating flow. From this construction we will be able to identify and understand spatio-temporal transport routes associated with different configurations of the front-eddy system by following the time evolution of the so-called *lobes* (cf. §3.2 and Appendix A.4). The geometry of lobes associated with different Lagrangian structures present in the flow will also give us the means for determining whether an 'interaction' between coexisting coherent structures actually takes place.

Dynamical systems theory is often described as the study of the 'long time' or asymptotic behaviour of systems. Indeed, the notions of hyperbolicity and stable and unstable manifolds of hyperbolic trajectories are concepts that are defined in the limit as time goes to plus

[1] In fluid mechanical terminology the phrase "invariant manifold" is synonymous with 'material surface' (in our setting the surface is a curve) and 'stable and unstable' refer to the behaviour of trajectories on the appropriate material surface, which we will describe shortly.

or minus infinity. Hence, these notions would appear to be somewhat problematic when considering applications to time-dependent velocity fields that are only defined for a finite time. The original applications of dynamical systems theory to the study of transport in flows was for two dimensional time-periodic or three-dimensional steady flows (for some history see [1, 45, 32]). The case for applying this approach to the study of Lagrangian transport in geophysical flows defined as data sets obtained from either numerical computation or experimental measurement is compelling, and it has necessitated the development of the notion of a 'finite-time dynamical system'. In this setting notions of finite-time hyperbolic trajectories and finite-time stable and unstable manifolds have been proposed (see, e.g., [35, 21, 17, 9, 23, 31]). Such notions have proven to give useful insight and quantitative predictions in geophysical flows (cf. the 'story of the jet' discussed in the introduction, and considered in some detail in [45, 32, 41]). The main difference between these finite-time concepts and their infinite-time counterparts is a loss of uniqueness of relevant hyperbolic structures that arises from the inability to consider asymptotic limits[2]. This implies, in particular, that the finite-time stable and unstable manifolds associated with any hyperbolic trajectory in an unsteady 2D flow on a finite time interval have the dimension of the extended phase space (x, y, t) (rather than a lower dimension). These issues are discussed in [14, 35, 21, 17, 9, 23, 31]. For our analysis this is not really a severe limitation since our finite-time hyperbolic trajectories are fluid particle trajectories. Consequently, the particular finite-time stable and unstable manifolds that we compute for these trajectories are "material surfaces" in the extended phase space (x, y, t) and we show directly their relevance to transport in the front-eddy system[3].

3.1 Working definition of a Lagrangian eddy.

Identification of eddies, or vortices, in flows is a topic that has received a great deal of attention in the fluid dynamics literature; [20] contains a recent discussion of the issues as well as a survey of the literature (but see also [38, 3, 10, 18, 25]). We seek a "working definition" of a Lagrangian eddy which will enable us to determine when such a structure is present in the flow of interest and the manner in which fluid is entrained and detrained by the eddy. Our construction exploits the fact that, in contrast to steady two-dimensional flows, the *stable and unstable* manifolds of *hyperbolic trajectories* (see Appendix A.3) in unsteady flows are time-dependent and, at any fixed time instant, they can intersect at isolated points within the flow domain. For our purposes a Lagrangian eddy will be a region bounded by intersecting segments of stable and unstable manifolds of hyperbolic trajectories with the resulting swirling sense of motion (clockwise or anticlockwise) on the boundary induced by the motion of trajectories making up the boundary segments. Figure 3 is an example of a Lagrangian eddy constructed in this way using, respectively, one hyperbolic trajectory (top row in figure 3) and two hyperbolic trajectories (bottom row in figure 3). Both these examples show the instantaneous eddy (and manifold) geometry so that each point on the plotted lines corresponds to an instantaneous location of a different trajectory.

At any time instant $t = t_i$, the boundary $\mathcal{B}_i$ of the single DHT eddy is made up of a segment of the unstable manifold $W^u_{\gamma_1}\{\boldsymbol{\gamma}_1(t_i), \boldsymbol{p}_i\}$ and a segment of the stable manifold

[2]Of course, one could argue that practically one realizes these notions through a numerical computation, which is necessarily a finite-time realization. However, making this assertion mathematically precise requires some considerable work that is beyond the scope of this paper, and much of which has not yet been undertaken (but see [19]).

[3]To avoid confusion with the classical, infinite time, notions of hyperbolicity and stable and unstable manifolds from dynamical systems theory one might think it would be less confusing to adopt new names for the analogous notions in the finite-time setting. Perhaps this would be a better approach, but at this point the terminology is fairly pervasive throughout the literature and new terminology could be even more confusing. In [41] an attempt is made to deal with this through the use of the phrase "material manifold", and this precisely describes a key feature of the relevance of these curves to fluid transport.

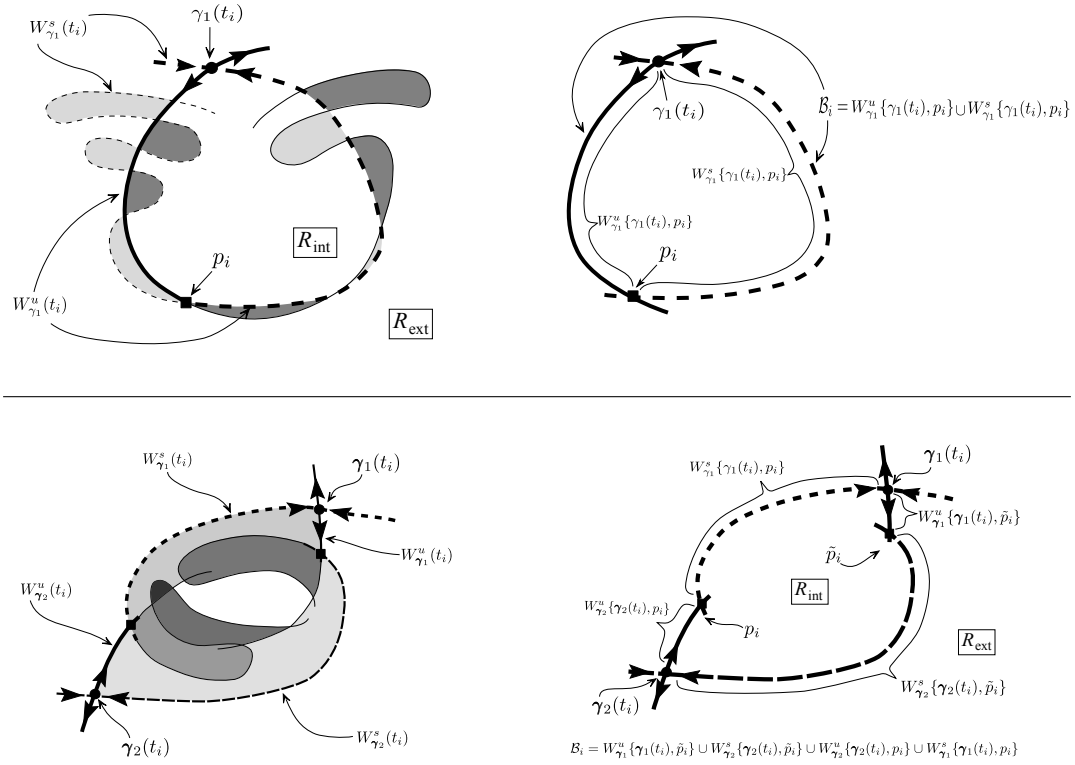

Figure 3: Schematic construction of a (time-dependent) boundary, $\mathcal{B}_i$, of a Lagrangian eddy using stable and unstable manifolds of a single DHT, $\boldsymbol{\gamma}_1(t)$ (top row), and two DHTs, $\boldsymbol{\gamma}_1(t)$, $\boldsymbol{\gamma}_2(t)$ (bottom row). At the time instant, $t = t_i$, the boundary of the single DHT eddy is made up of a segment of the unstable manifold $W^u_{\gamma_1}\{\boldsymbol{\gamma}_1(t_i), \boldsymbol{p}_i\}$ and a segment of the stable manifold $W^s_{\gamma_1}\{\boldsymbol{\gamma}_1(t_i), \boldsymbol{p}_i\}$ which intersect at the *boundary intersection point* $\boldsymbol{p}_i$. The boundary of the two-DHT eddy involves two bip's, $\boldsymbol{p}_i$, $\tilde{\boldsymbol{p}}_i$, and four distinct manifold segments: $W^u_{\gamma_1}\{\boldsymbol{\gamma}_1(t_i), \tilde{\boldsymbol{p}}_i\}$, $W^s_{\gamma_2}\{\boldsymbol{\gamma}_2(t_i), \tilde{\boldsymbol{p}}_i\}$, $W^u_{\gamma_2}\{\boldsymbol{\gamma}_2(t_i), \boldsymbol{p}_i\}$, $W^s_{\gamma_1}\{\boldsymbol{\gamma}_1(t_i), \boldsymbol{p}_i\}$. These eddies can exchange mass with the exterior region R_{ext} through lobes delineated by intersecting segments of the stable and unstable manifolds of the DHTs. Characteristics of the Lagrangian transport mediated by these lobes depend on the manifold geometry (see §3.2 and Appendix A.5 for more details).

$W^s_{\gamma_1}\{\boldsymbol{\gamma}_1(t_i), \boldsymbol{p}_i\}$ which intersect at the *boundary intersection point* $\boldsymbol{p}_i$ (see Appendix A.5 for more details); i.e. the boundary $\mathcal{B}_i$ at time t_i is given by

$$\mathcal{B}_i \;=\; W^u_{\gamma_1}\big\{\boldsymbol{\gamma}_1(t_i), \boldsymbol{p}_i\big\} \cup W^s_{\gamma_2}\big\{\boldsymbol{\gamma}_2(t_i), \boldsymbol{p}_i\big\}. \tag{1}$$

The boundary of the two-DHT eddy involves two bip's, $\boldsymbol{p}_i$, $\tilde{\boldsymbol{p}}_i$, and four distinct manifold segments: $W^u_{\gamma_1}\{\boldsymbol{\gamma_1}(t_i), \tilde{\boldsymbol{p}}_i\}$, $W^s_{\gamma_2}\{\boldsymbol{\gamma}_2(t_i), \tilde{\boldsymbol{p}}_i\}$, $W^u_{\gamma_2}\{\boldsymbol{\gamma}_2(t_i), \boldsymbol{p}_i\}$, $W^s_{\gamma_1}\{\boldsymbol{\gamma}_1(t_i), \boldsymbol{p}_i\}$.

The motion on the material boundary, induced by the evolution of the trajectories contained within the segments of the invariant manifolds, is counterclockwise in the single DHT configuration and clockwise in the two DHT case (see also Appendix A.5 and figure 18). This construction of an eddy was used earlier in [21], where the name *dynamic eddy* was proposed, and in [32] to describe the Lagrangian transport associated with the interaction of an eddy with a jet. We remark that most procedures that identify eddies in the recent oceanographic data sets are Eulerian in nature, e.g. [7] uses the Okubo-Weiss criteria. It is an interesting question to relate our Lagrangian construction of an eddy and the other criteria described

above. However, this is an extensive research topic in its own right and well beyond the scope of this paper.

3.2 Lobes and Lagrangian transport.

Lobes are formed from intersecting pieces of stable and unstable manifolds of hyperbolic trajectories (see, for example, the shaded areas in figure 3). We recall some basic definitions and lobe properties in Appendix A.4. (A more detailed discussion of this well-established notion can be found, for example, in [29, 32, 41].) The evolution of lobes can be used to understand the spatio-temporal mechanism for long range transport away from localized flow structures (eg. an oceanic front or an eddy).

Lobes associated with different Lagrangian structures in a flow can overlap. Since the lobes are flow invariant, their intersections are also invariant which implies that overlapping lobes will remain 'interlocked' throughout the flow evolution[4]. This lobe 'interaction' will play a crucial role in our Lagrangian analysis, giving rise to much more complex transport templates.

Historically, special lobes, called 'turnstiles', were considered as the main building blocks supporting the mechanism for crossing the time-dependent boundary, $\mathcal{B}(t)$ (cf. §3.1). The basics of the construction for aperiodic time-dependence and finite time given in [29, 41]. The background and history of this notion can be found in [32] (relevant references for the original work for area-preserving maps are [6, 2, 27]). In the following analysis we also identify a different transport mechanism which operates intermittently in one of the eddies in the analysed flow. Two examples of distinct manifold geometry, resulting in different transport properties are sketched in figure 3. The manifold geometry shown in the single DHT case corresponds to the 'traditional' turnstile mechanism (this geometry can be also realised in the two-DHT case; see figure 19). The important feature of manifold geometry can be summarised as follows. Consider a collection of successive intersection points, $\boldsymbol{p}_i$, $\boldsymbol{k}_i$, $\boldsymbol{l}_i$, between a stable manifold $W^s_{\gamma_1}$ and an unstable manifold $W^u_{\gamma_2}$ at time t_i such that

$$W^s_{\gamma_1}\{\boldsymbol{\gamma_1(t_i)},\boldsymbol{p_i}\} < W^s_{\gamma_1}\{\boldsymbol{\gamma_1(t_i)},\boldsymbol{k_i}\} < W^s_{\gamma_1}\{\boldsymbol{\gamma_1(t_i)},\boldsymbol{l_i}\}. \tag{2}$$

If the following holds

$$W^u_{\gamma_2}\{\boldsymbol{\gamma_2(t_i)},\boldsymbol{p_i}\} > W^u_{\gamma_2}\{\boldsymbol{\gamma_2(t_i)},\boldsymbol{k_i}\} > W^u_{\gamma_2}\{\boldsymbol{\gamma_2(t_i)},\boldsymbol{l_i}\}, \tag{3}$$

then the turnstile lobes are formed (as sketched in the top row of figure 3). If, on the the hand

$$W^u_{\gamma_2}\{\boldsymbol{\gamma_2(t_i)},\boldsymbol{p_i}\} < W^u_{\gamma_2}\{\boldsymbol{\gamma_2(t_i)},\boldsymbol{k_i}\} < W^u_{\gamma_2}\{\boldsymbol{\gamma_2(t_i)},\boldsymbol{l_i}\}, \tag{4}$$

as in the two-DHT case shown in figure 3, a different 'tumbling' mechanism is at play. We will show in the following sections that both these transport mechanisms are important in our flow. We postpone a more detailed discussion of different manifold geometries leading to these distinct transport mechanisms to the Appendix A.5.

4 Lagrangian structures and transport in the front-eddy system

Transport across an oceanic front, identified in the North-Western Mediterranean Sea, was recently discussed in detail in [30]. In that work a 'leaky' Lagrangian transport barrier

[4]The flow invariance of material manifolds and lobes is, of course, only strictly satisfied for inviscid fluid flows.

(i.e. the front) between two disjoint regions of the flow domain, as well as a set of turnstile lobes mediating transport across it, were constructed from two invariant manifolds of two DHTs which were located at the two ends of the front. However, it was pointed out in [30] that the presence of strong eddies near the identified Lagrangian front could open up new transport pathways, introducing additional complexity to the spatio-temporal flow structure near the front, especially when following the flow evolution over time intervals longer than those considered in [30]. In order to take into account the existence of the additional long-lived flow structures, potentially interacting with the front, it is necessary to consider a more complicated manifold structure. We focus first on two different situations which involve an interaction of a Lagrangian front with one or two Lagrangian eddies (cf. §3.1). We refer to these two cases as, respectively, Scenario I and Scenario II. Such a choice was largely motivated by a careful inspection of the realistic flow data obtained for the North-Western Mediterranean Sea from the DieCAST model, already mentioned in §2. We stress that the distinction between the flow configurations associated with Scenario I and II is somewhat artificial since the analysed flow evolves intermittently between these two scenarios.

Our goal in this section is two-fold. First, we aim to understand transport processes acting in Scenarios I and II. We then allow for transitions between these two configurations which 'open-up' new, intermittent transport pathways and cannot be understood by considering the two scenarios separately. We also want to outline a general procedure for extracting the relevant Lagrangian information from the Eulerian velocity data associated with realistic, aperiodically time-dependent flows. Our analysis develops methods for understanding the essential features and basic building blocks that generate this complex spatio-temporal structure and its influence on Lagrangian transport.

4.1 Transport associated with the interaction of an Eulerian current with a single eddy

The Eulerian flow features which are often associated with the existence of the Lagrangian flow structure of Scenario I were highlighted earlier in figure 1 (see also figures 4, 5). It is generally impossible to predict with certainty that such a Lagrangian structure exists in a flow until the geometry of the relevant invariant manifolds is determined. As can be seen in figure 5, the manifolds in the tangle we associated with Scenario I belong to two DHTs (cf. Appendix A) which we refer to hereafter as the western DHT ($\mathcal{H}_W$) and the eastern DHT ($\mathcal{H}_E$). It is thus necessary that we first demonstrate the existence of these 'special' hyperbolic trajectories in the flow. This is not always a straightforward task, since we search for these DHTs using an iterative algorithm, described in [23], which requires a 'good' initial guess in order to converge. In the search process, we are usually guided by the Eulerian flow features, such as the hyperbolic ISPs, which remain near the ends, or near branching points, of the identified current. We usually use such paths of ISPs as the initial guesses in the DHT-finding algorithm. However, we remind the reader that any other frozen-time hyperbolic guess could be used in the algorithm, as long as it leads to its convergence to a hyperbolic trajectory (see §A and [24]).

Assuming that we located the required DHTs in the flow and computed sufficiently long segments of their (time-dependent) stable and unstable manifolds, we can analyse the Lagrangian transport processes associated with Scenario I, using the tools introduced in §A. In order to do that, we first need to identify the geometry of a (time-dependent) boundary between different regions present in the flow for an ordered sequence of 'observation times' $t_0 < t_1 < ... < t_N$. Here, we choose only a two element sequence $\{t_1, t_2\}$, which is sufficient to illustrate the construction of the boundary, as shown in figure 4, and to understand the action of the turnstile mechanism which mediates transport across different parts of this

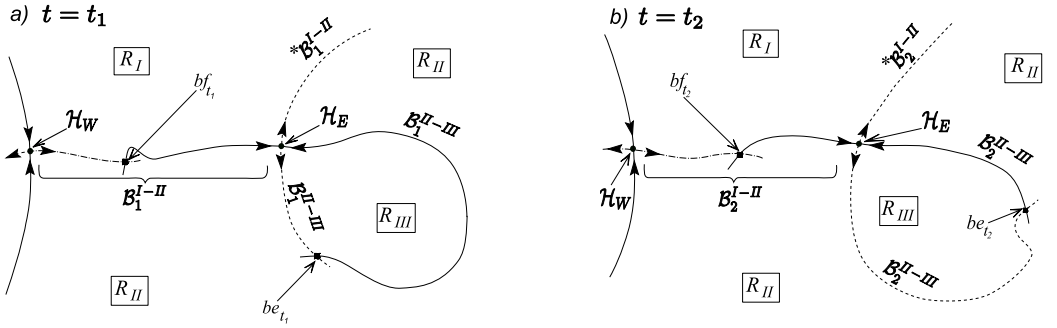

Figure 4: **Scenario I**. Construction of a time-dependent boundary, $\mathcal{B}^{I-III} \cup \mathcal{B}^{II-III}$, which involves invariant manifolds of two hyperbolic trajectories $\mathcal{H}_W$ and $\mathcal{H}_E$. The geometry at two 'observation' times (a) $t = t_1$ and (b) $t = t_2$ ($t_2 > t_1$) is sketched. We show only the manifold segments which are necessary to define the boundary at a given time. The intersection points of invariant manifolds used in the construction of the boundary (i.e. boundary intersection points) are denoted by bf_{t_1} and bf_{t_2} for the front, and by be_{t_1}, be_{t_2} for the eddy. The boundary divides the flow domain into three distinct regions: R_I, R_{II} and R_{III}.

boundary.

Construction of the boundary segment $\mathcal{B}^{I-II}$ coincides with that presented in [30] and relies on the fact that, generically, invariant manifolds of DHTs in unsteady flows intersect repeatedly (but this must be verified for specific data sets). This allows us to choose a sequence of boundary intersection points $\{bf_i\}$ (see §A and figures 18, 3), one for each time t_i, and define $\mathcal{B}_i^{I-II}$ as the union of the segment $W^u_{\mathcal{H}_W}\{\mathcal{H}_W, bf_{t_i}\}$ of the unstable manifold of $\mathcal{H}_W$ and of the segment $W^s_{\mathcal{H}_E}\{\mathcal{H}_E, bf_{t_i}\}$ of the stable manifold of $\mathcal{H}_E$ (cf. (1)). Hereafter, we refer to the segment $\mathcal{B}^{I-II}$ as the 'front', since its location is correlated with sharp gradients of salinity and temperature fields in the data (see [30]).

In order to capture additional transport features associated with the existence of the Lagrangian eddy at the eastern end of the front, we also have to take into account the geometry of the remaining branches of invariant manifolds of $\mathcal{H}_E$. The boundary between the eddy region and the surrounding flow at $t = t_i$, denoted as $\mathcal{B}_i^{II-III}$, is given by the union of two segments of invariant manifolds associated with $\mathcal{H}_E$: a segment of its unstable manifold, $W^u_{\mathcal{H}_E}\{\mathcal{H}_E, be_{t_i}\}$, and a segment of its stable manifold, $W^s_{\mathcal{H}_E}\{\mathcal{H}_E, be_{t_i}\}$, intersecting at the boundary intersection point be_{t_i} (see figure 4).

Consequently, at any time instant, we can distinguish three distinct regions in the flow domain, which are separated by Lagrangian barriers formed by the connected boundary segments $\mathcal{B}^{I-II}$ and $\mathcal{B}^{II-III}$. We denote the region to the North of the front by R_I, the interior of the eddy by R_{III}, and the region bordering the eddy from the South and the North-East by R_{II}. The analysis of transport between these regions requires different levels of complexity, depending on the transport route considered. In order to understand transport processes across the front or across the eddy boundary (i.e. the routes of the form $R_i \leftrightarrow R_j$), it is sufficient to analyse the evolution of simple turnstile lobes associated with the respective boundary segment (see figure 5). Understanding transport routes which arise due to the interaction between the front and the eddy requires taking into account those pairs of simple turnstile lobes, associated with the front and the eddy boundary, which overlap with each other (see figure 8). Finally, there are transport processes whose understanding requires the existence of the composite lobes in the underlying flow. Below, we discuss transport routes present in Scenario I and shown schematically in figure 14a in the order of increasing complexity.

Transport across the front ($R_I \leftrightarrow R_{II}$)

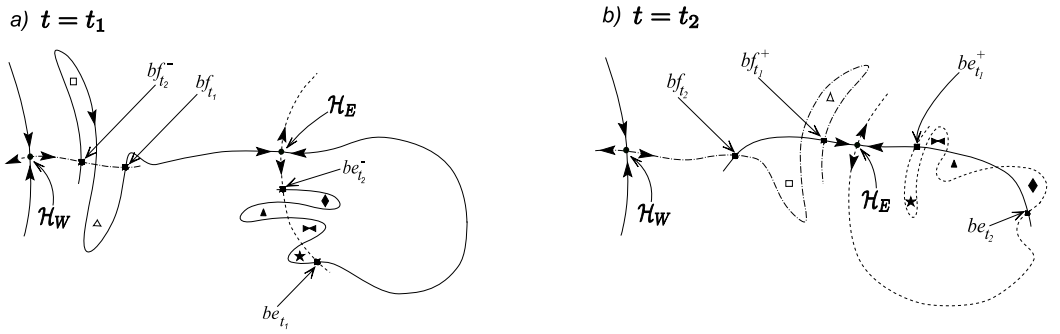

Figure 5: **Scenario I**. Schematic construction of turnstile lobes for the front and the eddy at (a) $t = t_1$ and their geometry after evolution to $t = t_2$ (b) (see also figure 4). The front turnstile lobes are defined as the lobes formed by segments of $W^u_{\mathcal{H}_W}$ and of $W^s_{\mathcal{H}_E}$ between the boundary intersection point ('*bip*') at $t = t_1$, denoted as bf_{t_1}, and the pre-image of the *bip* at $t = t_2$, denoted by $bf^-_{t_2} \equiv \boldsymbol{f}^{-1}_{t_1}(bf_{t_2})$. At $t = t_2$, bf_{t_1} evolves to $bf^+_{t_1} \equiv \boldsymbol{f}_{t_2}(bf_{t_1})$. The action of the flow-induced mapping $\boldsymbol{f}$, defined by (13), was illustrated in figure 18. The eddy multilobe turnstile, bounded by $be^-_{t_2}$ and be_{t_1} at $t = t_1$ is constructed in an analogous way. The squares, triangles and stars are to aid visualization of how the turnstile lobes evolve from t_1 to t_2.

The turnstile lobes associated with the front ($\mathcal{B}^{I-II}$) can be constructed in a standard way which was carried out earlier in [30]. We do so by considering the lobes formed at $t = t_1$ by the intersecting segments of $W^u_{\mathcal{H}_W}$ and $W^s_{\mathcal{H}_E}$ between two *primary intersection points*, bf_{t_1} and $bf^-_{t_2}$ (see figure 5), which satisfy the ordering under the flow evolution in the form $bf_{t_1} <_s bf^-_{t_2}$ (see figure 18). The point bf_{t_1} is the boundary intersection point at $t = t_1$ and the point $bf^-_{t_2}$ denotes the pre-image of the boundary intersection point at $t = t_2$ under the the volume- and orientation-preserving map $\boldsymbol{f}$ (cf. (13)), induced by the underlying flow (i.e. $bf^-_{t_2} \equiv \boldsymbol{f}^{-1}_{t_1}(bf_{t_2})$). An example of a two-lobe front turnstile constructed in this way is shown in figure 5a (see the lobes marked by "□" and "△"). Provided that the next observation time t_2 is chosen in such a way that the turnstile is advected sufficiently close to $\mathcal{H}_E$, under the action of $\boldsymbol{f}$, the two front lobes must evolve in the way shown in figure 5b which results in a transfer of fluid particles confined within these lobes across the front.

In order to show the existence of such a transport route in the aforementioned flow in the North-Western Mediterranean Sea (cf. §2), we show in figure 6 the computed geometry of the relevant invariant manifolds in the flow at day 664 and day 683. The blue curves mark there the stable manifold of the eastern DHT ($\mathcal{H}_E$) and the red curve denotes the unstable manifold of the western DHT ($\mathcal{H}_W$). The two sets of coloured dots mark locations of a fixed number of conveniently chosen fluid-particle trajectories at the two time instants, and are to aid the visualisation of transport across the front. The magenta-coloured dots mark fluid particles confined to northern lobes, i.e. the lobes originating close to $W^s_{\mathcal{H}_W}$ north of the front segment $\mathcal{B}^{I-II}$ in figure 6a). The green-coloured dots mark fluid particles confined to southern lobes (i.e. the lobes originating close to $W^s_{\mathcal{H}_W}$ south of the front on day 664). At the later stage of the evolution, shown in figure 6b, the northern lobes containing the magenta dots end up south of the front and the southern lobes containing the green dots have migrated to the north of the front by day 683.

Transport in and out of the eddy ($R_{II} \leftrightarrow R_{III}$)

The basic transport mechanism across the boundary of the eddy region ($\mathcal{B}^{II-III}$) can be described in a way analogous to the one developed for the transport across the front although, in this case, the existence of homoclinic tangles (rather than heteroclinic tangles) is needed for transport across this boundary segment to take place. We note here that this transport

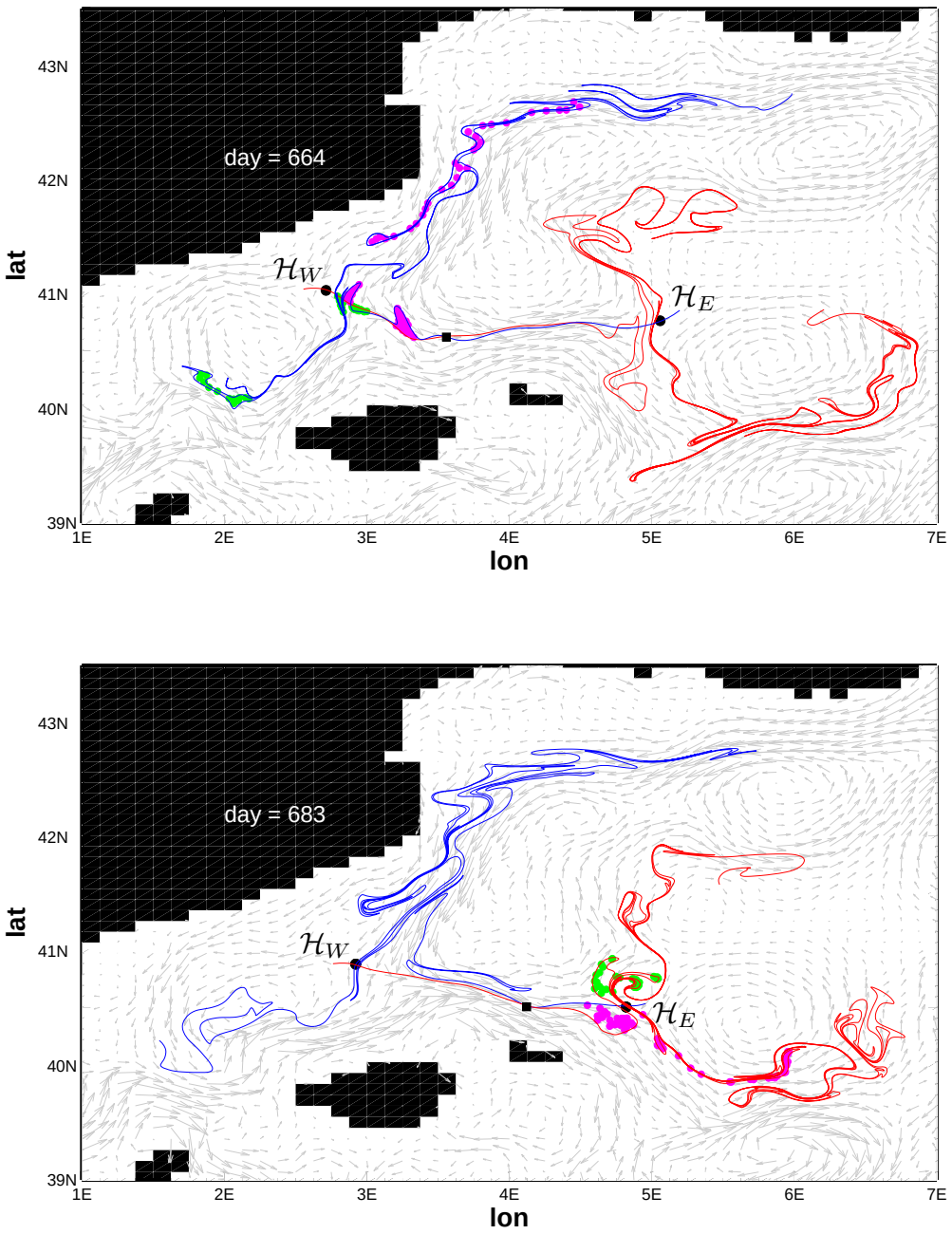

Figure 6: **DieCAST model, NW Mediterranean.** Transport across the Lagrangian front (see the segment $\mathcal{B}^{I-II}$ in figures 4, 10) between days 664 and 683 illustrated by following the evolution of a set of trajectories which originate in lobes located initially to the South of the front (green; region R_{II}) and in lobes to the North of the front (magenta; region R_I). This transport route acts in the way sketched in figures 5 and 11 (see the lobes $\square$, $\triangle$). Justification of the 2D analysis is presented in Appendix **??**.

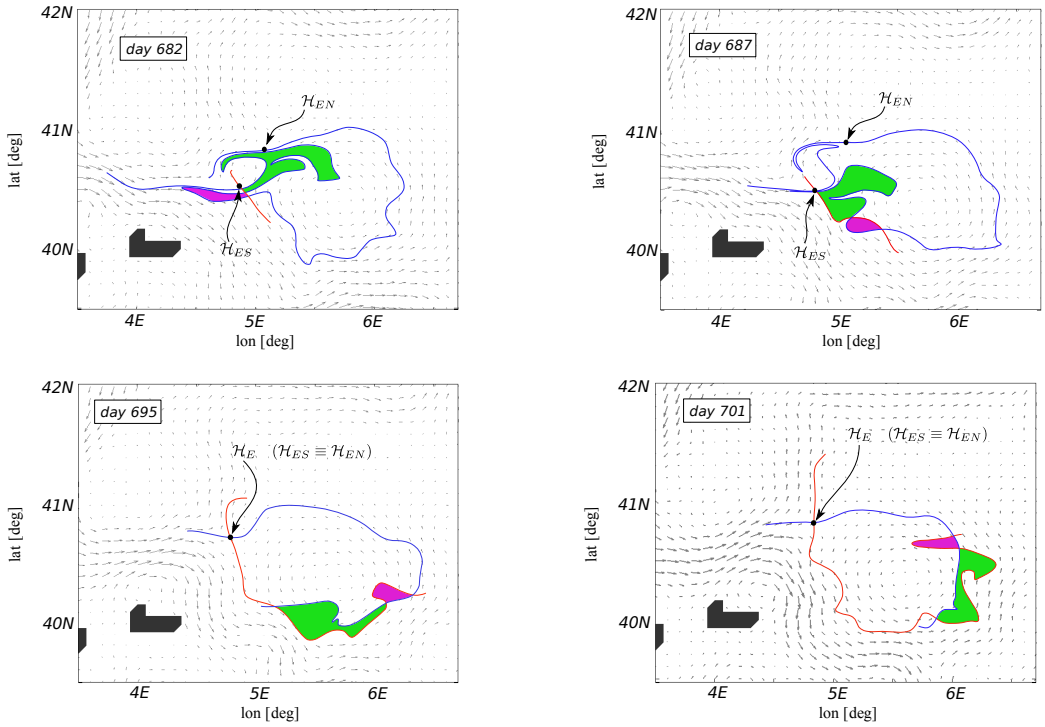

Figure 7: **DieCAST model, NW Mediterranean.** Transport across the eddy boundary (segment $\mathcal{B}^{II-III}$ in figures 4, 10) between days 682 and 701 illustrated using a two-lobe turnstile (compare with figure 5). The red and blue curves mark, respectively, the unstable and stable manifolds of the hyperbolic trajectory denoted by the black dot. The black squares denote the boundary intersection points.

route is also present in Scenario II and it remains active even if the flow structure evolves intermittently between Scenarios I and II. We construct the relevant simple turnstile lobes by considering the lobes formed by the intersecting segments of $W^u_{\mathcal{H}_E}$ and $W^s_{\mathcal{H}_E}$ between the pre-image of the *bip* at $t = t_2$, denoted as $bf^-_{t_2} = f^{-1}_{t_1}(bf_{t_2})$, and the boundary intersection point bf_{t_1} (see the lobes marked by ▲, ★, ⋈, ♦ in figure 5). The evolution of such lobes is governed, as before, by the volume- and orientation-preserving map $\boldsymbol{f}$ induced by the flow. The invariance of the manifold intersection points under the action of $\boldsymbol{f}$ implies that at $t = t_2$ these lobes are bounded by the segments of invariant manifolds between bf_{t_2} and $bf^+_{t_1} = \boldsymbol{f}_{t_2}(bf_{t_1})$, as shown in figure 5b.

Assuming that the relevant Lagrangian flow structure is fully captured by Scenario I (i.e. there are no intersections between $\mathcal{B}^{II-III}$ and stable or unstable manifolds of other DHTs), the eddy turnstile lobes are advected away from $\mathcal{H}_E$ in a counter-clockwise sense around the perimeter of the large eddy region R_{III} until they re-approach $\mathcal{H}_E$ along $W^s_{\mathcal{H}_E}$. By then, the eddy lobes which were initially located in R_{II} (see ▲, ★) are entrained into the eddy region and the lobes which originated inside the eddy at $t = t_1$ (see ⋈, ♦) are ejected to R_{II} and stretched into long filaments along the unstable manifold of $\mathcal{H}_E$ (see figure 5b).

Note also that fluid particles located south of the front at $t = t_1$ (in the region R_{II}) but not contained in the eddy lobes will travel around the perimeter of the eddy region without being entrained into R_{III}, and then proceed to the North along the unstable manifold of $\mathcal{H}_E$. This transport route is sketched in figure 14 as the outermost blue path, located outside R_{III} (note that this route is also present in Scenario II). Whether a fluid particle is advected around exterior of the eddy to the North, or whether it is entrained first into the eddy region

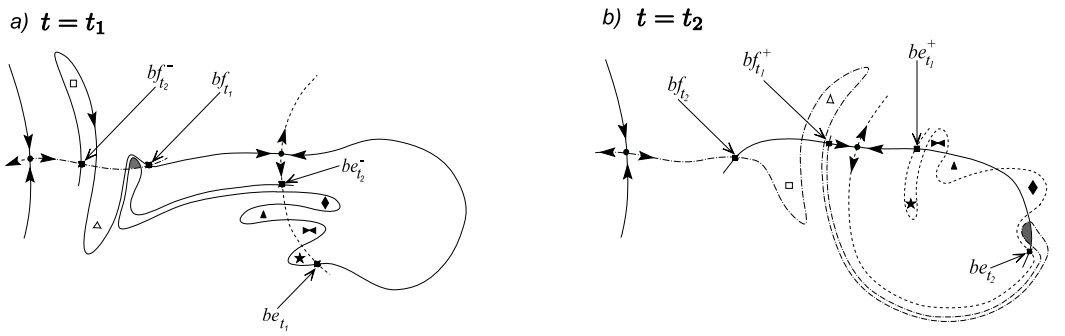

Figure 8: **Scenario I**. Illustration of an interaction between the front lobes and the eddy lobes (note that the *bip* at t_1 (i.e. bf_{t_1}) is defined differently to that of figure 4 in order to visualise the interaction). (a) initial geometry showing a lobe associated with the eddy boundary (i.e. $\mathcal{B}^{II-III}$ in figure 4) overlapping with one of the lobes associated with the front; (b) the overlap area (shaded) is entrained into the eddy by $t = t_2$ (the eddy boundary at t_2 is defined in Fig. 4b).

and rapidly stirred before exiting to the North is very sensitive to the spatial and temporal location of the particle (i.e. it depends on which lobe it is in).

We now illustrate this transport route in the same front-eddy system which we identified earlier in the North-Western Mediterranean Sea (figures 1, 2), and which we used to illustrate the transport across the front (figure 6). We note that within the time intervals required to observe the turnstile transport mechanism across the eddy boundary the Lagrangian flow structure often evolves intermittently between Scenarios I and II (see figure 17). However, as can be seen from our construction shown in figures 5 and 11, the short-term transport across the boundary segment $\mathcal{B}^{II-III}$ remains unchanged regardless of whether the flow evolves according to Scenario I or Scenario II. We discuss the effect of this transitions on transport in more details in §4.3.

Figure 7 shows the computed geometry of the relevant invariant manifolds of $\mathcal{H}_E$ whose segments make up the large, time-dependent eddy region at the eastern end of the front (see R_{III} in figures 4, 10). The four snapshots shown in the insets correspond to days 682, 687, 695 and 701 in the simulation. The boundary intersection point at each of these times is marked by the black square and the stable and unstable manifolds of $\mathcal{H}_E$ are colour-coded in the same fashion as in figure 6 (i.e. red - the unstable manifold, blue the stable manifold). We highlight in this figure an evolution of a two-lobe turnstile associated with the eddy boundary $\mathcal{B}^{II-III}$ (see figure 4) by using the green- and magenta-coloured dots to mark locations of a fixed set of fluid particles. The green-coloured particles are confined within a lobe which initially, on day 682, was located inside R_{III}. These particles are expelled from the eddy region around day 695, as illustrated in figure 7c. At the same time, the fluid particles (magenta) confined within the eddy turnstile lobe located initially (day 682, figure 7a) in R_{II} are entrained into R_{III}, as shown in figure 7c,d.

Note that the transport processes responsible for mass exchange across the Lagrangian front and across the boundary of the Lagrangian eddy would persist if we considered each of these flow structures in isolation. However, if the two structures interact with each other, additional transport routes open up in the flow, leading to enhanced tracer stirring in the combined system. We discuss these additional transport routes below.

Transport routes arising due to front-eddy interaction ($R_I \to R_{II} \to R_{III}$)

The simple-turnstile mechanism outlined above is not capable of describing transport

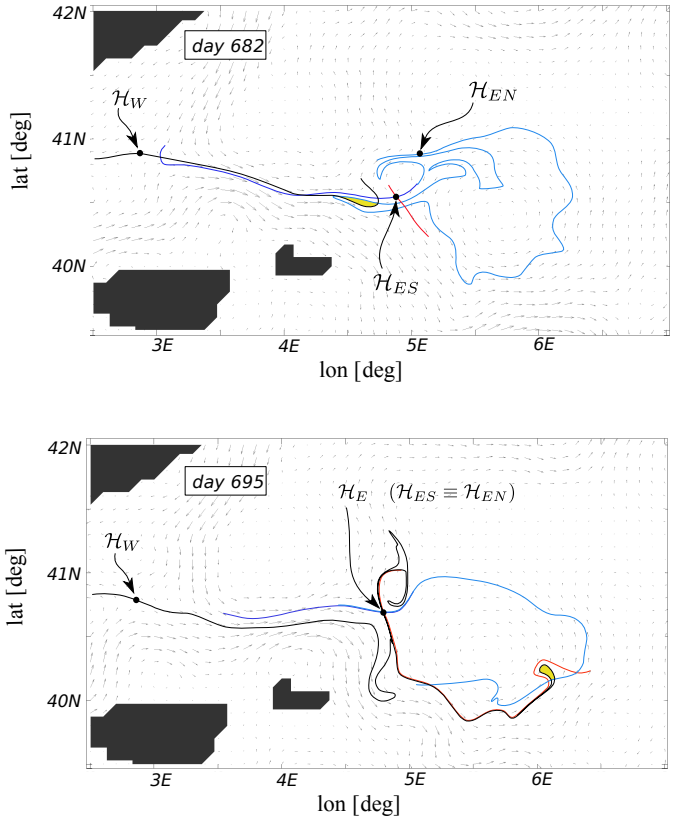

Figure 9: **DieCAST model, NW Mediterranean.** Interaction of the Lagrangian front with the large eddy manifested by an intersection of a front turnstile lobe with an eddy lobe (yellow-shaded area). Water contained within the intersecting area can be traced back to cold water lobes which originate in the North (see the magenta dots with figure 6 and the "□"-lobe in figures 5, 11). This volume of water is entrained into the large eddy across the boundary segment $\mathcal{B}^{II-III}$ inside a simple eddy lobe, according to the mechanism shown in figures 5, 11.

processes arising through the interaction of the front end the eddy. In order to determine whether or not a fluid (or tracer) particle which crossed the front from the North in a front lobe is subsequently going to be entrained into the large eddy region, one has to determine if this particle is also contained in one of the lobes associated with the eddy. Such a procedure usually requires examining simple turnstile lobes which have much larger arc lengths than those considered before. The necessary condition for an interaction between two distinct Lagrangian structures, which is manifested by mass transport across their respective boundaries, is the overlap between at least one pair of lobes belonging to each of these structures. In other words, we say that two (localised) Lagrangian flow structures, say A and B, interact if at least one lobe associated with A intersects at least one lobe associated with B. The invariance of the manifold intersection points under the flow induced map $\boldsymbol{f}$ implies then that a tracer captured within the intersecting area remains confined within it for all time (assuming no diffusion), which results in an entrainment of the intersecting part of the lobe associated with A inside B or vice versa. We note that this phenomenon has been observed before, for example in [32], although it was not explicitly defined.

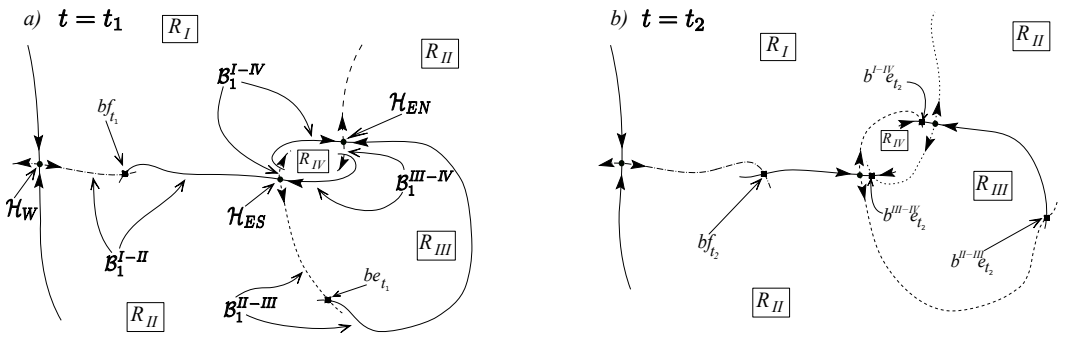

Figure 10: **Scenario II**. Construction of a time-dependent boundary, $\mathcal{B}^{I-III} \cup \mathcal{B}^{II-III} \cup \mathcal{B}^{I-IV} \cup \mathcal{B}^{III-IV}$, which separates distinct regions in the flow (R_I, R_{II}, R_{III} and R_{IV}) at two different 'observation' times (*a*) $t = t_1$ and (*b*) $t = t_2$. R_{III} denotes the large eddy region, which is also present in Scenario I, and R_{IV} marks the emergent small-eddy region. Compare this geometry with that of Scenario I shown in figure 4. Transport across this boundary can be analysed by considering turnstile lobes shown in figure 11.

In order to illustrate the interaction between a northern front lobe (i.e. a lobe associated with $\mathcal{B}^{I-II}$ which originates in R_I) and an eddy turnstile lobe, we change the location (with respect to that of figure 4a) of the boundary intersection points, bf_{t_1} and be_{t_1}, as shown in figure 8a. As a consequence, one of the lobes in the eddy turnstile now stretches over distances comparable with the characteristic length of the front and intersects with one of the front turnstile lobes (shaded area). Evolution of these turnstiles to $t = t_2$ results in the entrainment of a portion of the front lobe into the eddy region (see figure 8b). Note that only the northern lobes, i.e. the lobes that can be inverse-mapped to R_I using $\boldsymbol{f}$ (cf. 13), can be entrained into the eddy region R_{III} during such a process.

In [30] the turnstile mechanism for cross-frontal transport generates filaments of cold and less salty water protruding into the warmer and saltier region South of the front. If the geometry of the relevant manifolds is such that the eddy turnstile lobes intersect with the front turnstile lobes, as sketched earlier in figure 8, the flow evolution will first bring the cold-water, northern front lobe, containing the intersecting area, South of the front (to region R_{II}) and then into the large eddy. Such a scenario is indeed observed in the front-eddy system we identified in the North-Western Mediterranean Sea. We illustrate this process in figure 9 where the shaded area can be traced back in time to one of the lobes originating in the North (see figures 6 and 8).

4.2 Additional transport routes associated with the emergence of the second eddy in the front-eddy system

The evolution of the velocity field obtained from the DieCAST ocean circulation model (cf. §2) for the North-Western Mediterranean Sea is characterised by an intermittent emergence and disappearance of an additional smaller Eulerian eddy at the eastern end of the front, as illustrated earlier in figures 1 and 2. The evolution of the associated temperature field indicates that the presence of the second Eulerian eddy is often correlated with an injection of warm-water filaments into the large eddy region from the North, across the small eddy, and that such a process is not present when the small eddy disappears. The appearance of this additional transport route indicates indirectly a change in the underlying Lagrangian flow structure with respect to Scenario I (see figures 10, 11) where such a transport process cannot be realised. We develop here the Lagrangian characterisation of a front-eddy system

which is composed of two Lagrangian eddies interacting with the front. We refer to such a flow geometry as Scenario II and describe the Lagrangian mechanism responsible for the entrainment of warm water filaments into the large eddy region across the small eddy region. We later show, in §4.3, show how these two Lagrangian structures (i.e. Scenario I and II) can evolve between each other.

The emergence of the additional Eulerian eddy at the end of the front is accompanied by a saddle-node bifurcation of the ISP path which was earlier used to locate $\mathcal{H}_E$ in §4.1. This bifurcation produces an elliptic ISP, which we associate with the birth of the new Eulerian eddy, and a new hyperbolic ISP. The newly created path of the hyperbolic ISPs can be used as an initial guess in the DHT-finding algorithm [23] in an attempt to determine whether a new DHT exists in the flow, alongside the previously located DHTs which enabled us to recognise the manifold geometry of Scenario I. If such a procedure does indeed lead to the identification of the additional DHT, the underlying structure of the intersecting invariant manifolds of the three DHTs forms a tangle which is rather different than the one associated with the Lagrangian geometry of Scenario I (see figures 5 and 11).

In what follows, we will denote the DHT on the western end of the front as $\mathcal{H}_W$, as in the description of Scenario I, and the two remaining DHTs by $\mathcal{H}_{NE}$ and $\mathcal{H}_{SW}$, according to their relative geographical location (see figure 10). For this geometry, in addition to the previously identified disjoint regions in the flow domain, R_I, R_{II} and R_{III}, we can distinguish a fourth region, denoted as R_{IV}, corresponding to the small eddy region (see figure 10).

The boundary in this scenario is constructed in a similar way to that described for Scenario I in §4.1. We illustrate this process in figure 10. In addition to the front and the large eddy boundary intersection points, denoted by bf_{t_i} and $be_{t_i}^{II-III}$ respectively, we need to specify two additional *bips* on the boundary of the small eddy region R_{IV}, denoted by $be_{t_i}^{I-IV}$ and $be_{t_i}^{III-IV}$.

All of the transport routes discussed in the context of Scenario I are also present in Scenario II (see figure 14). In figure 11 we illustrate the construction of the appropriate simple turnstile lobes which mediate transport across different parts of the boundary.

There also exists new transport routes for this geometry which arise due to the presence of the two new boundary segments, $\mathcal{B}^{I-IV}$ and $\mathcal{B}^{III-IV}$. The simple turnstile lobe transport mechanism across these segments is illustrated in the insets of figure 11 (see the lobes marked by "✖✖", "✖", "▼▼" and "▼" in figure 11).

These transport routes can be observed in the flow field data obtained from the DieCAST model (§2) which we illustrate in figure 12. The presented sequence of instantaneous geometry snapshots illustrates entrainment of a lobe (light blue) from region R_I into R_{IV} across the small eddy in the way sketched earlier in figure 11. Since the small eddy region exists in the studied flow for relatively short periods of time (i.e. it emerges and disappears several times in the available data set), we were able to detect a single lobe being entrained into the small eddy and a single lobe being ejected out of it (the geometry of the DHTs during the examined episode is shown in figure 17). Note that the transport mechanism which is active here is not the turnstile mechanism and that the light and dark blue lobes end up spread in distinct regions (i.e. light blue lobe in region R_{III} and the dark blue lobe in R_I) as a consequence of this mechanism.

Finally, in figure 13, we show an evidence of interaction of lobes associated with different Lagrangian structures in the flow in the North-Western Mediterranean Sea. This mechanism is responsible for transporting some of the warm water filaments, originating in R_{II}, across the front and then into the large eddy region R_{III} through the small eddy R_{IV}. The black curve shown in figure 13 shows the geometry of the computed unstable manifold of $\mathcal{H}_W$. The yellow-shaded region marks an overlap between a front lobe and a small eddy lobe. The front lobe formed by the intersecting segments of $W^u_{\mathcal{H}_W}$ and $W^s_{\mathcal{H}_{ES}}$ contains warm water

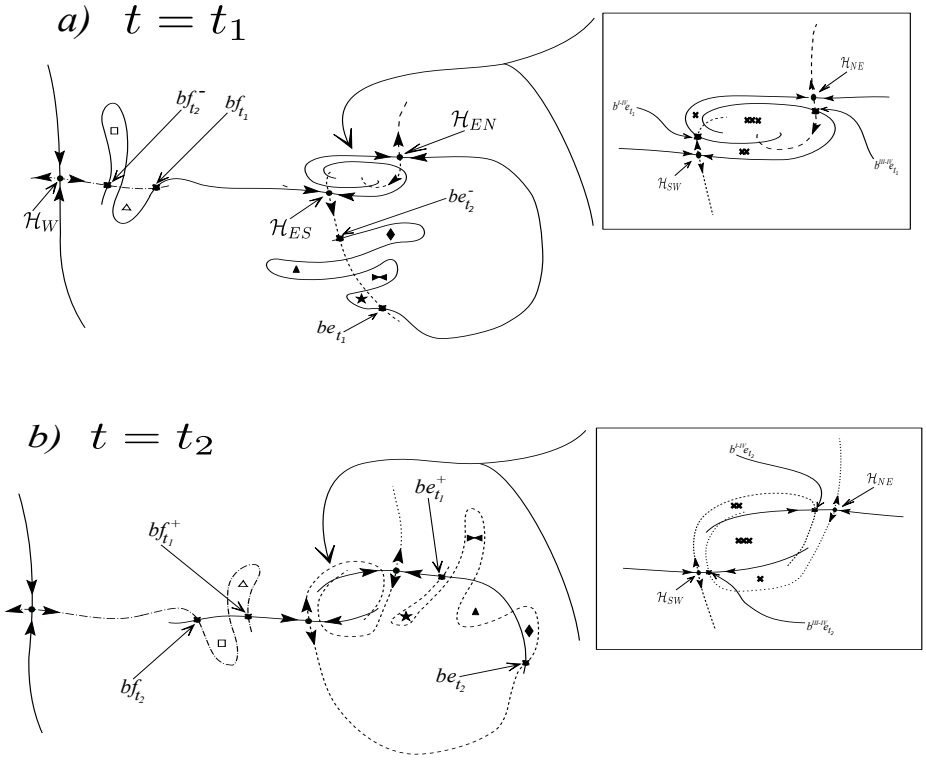

Figure 11: **Scenario II**. Schematic evolution of 'simple' turnstile lobes (i.e. lobes which do not overlap with other lobes) from $t = t_1$ to $t = t_2$. Transport across the front (see $\mathcal{B}^{I-II}$ in figure 10) and across the boundary segment $\mathcal{B}^{II-III}$ of the large eddy region is the same as in Scenario I. Transport across the boundary of the emergent small eddy region is illustrated in the insets.

transported earlier across the front from the South (i.e. $R_{II} \to R_I$ across $\mathcal{B}^{I-II}$), according to the previously described simple lobe turnstile mechanism of cross-frontal transport. The overlapping area (yellow) between the front lobe and a small eddy lobe, is first entrained into the small eddy region (figure 13b) and subsequently ejected into the large eddy region (figure 13d).

In figure 14 we summarise the transport mechanisms discussed in the two previous sections in relation to Scenarios I and II by sketching transport routes of a tracer contained in northern lobes (blue; lobes that can be inverse mapped in time to the region R_I) and in southern lobes (green; lobes that can be inverse mapped in time to the region R_{II}). We assume here that the Lagrangian configurations of Scenario I or Scenario II exist in the flow for times long enough that all the indicated transport routes can be accomplished. If the Lagrangian flow structure evolves 'too rapidly' between the two configurations, or if it changes to a completely different structure, some of these routes may be terminated prematurely. Note finally that additional transport routes, not present in Scenarios I and II, might appear in the flow if the front-eddy system interacts significantly with other Lagrangian flow structures. For example, while following the evolution of a lobe associated with the large eddy (R_{III}), just like the one shaded in figure 9a, one could observe this lobe (or part of it) to travel South-West instead of moving counterclockwise around the perimeter of the large eddy. The turnstile mechanism for transport associated with the invariant manifolds considered in Scenarios I and II does

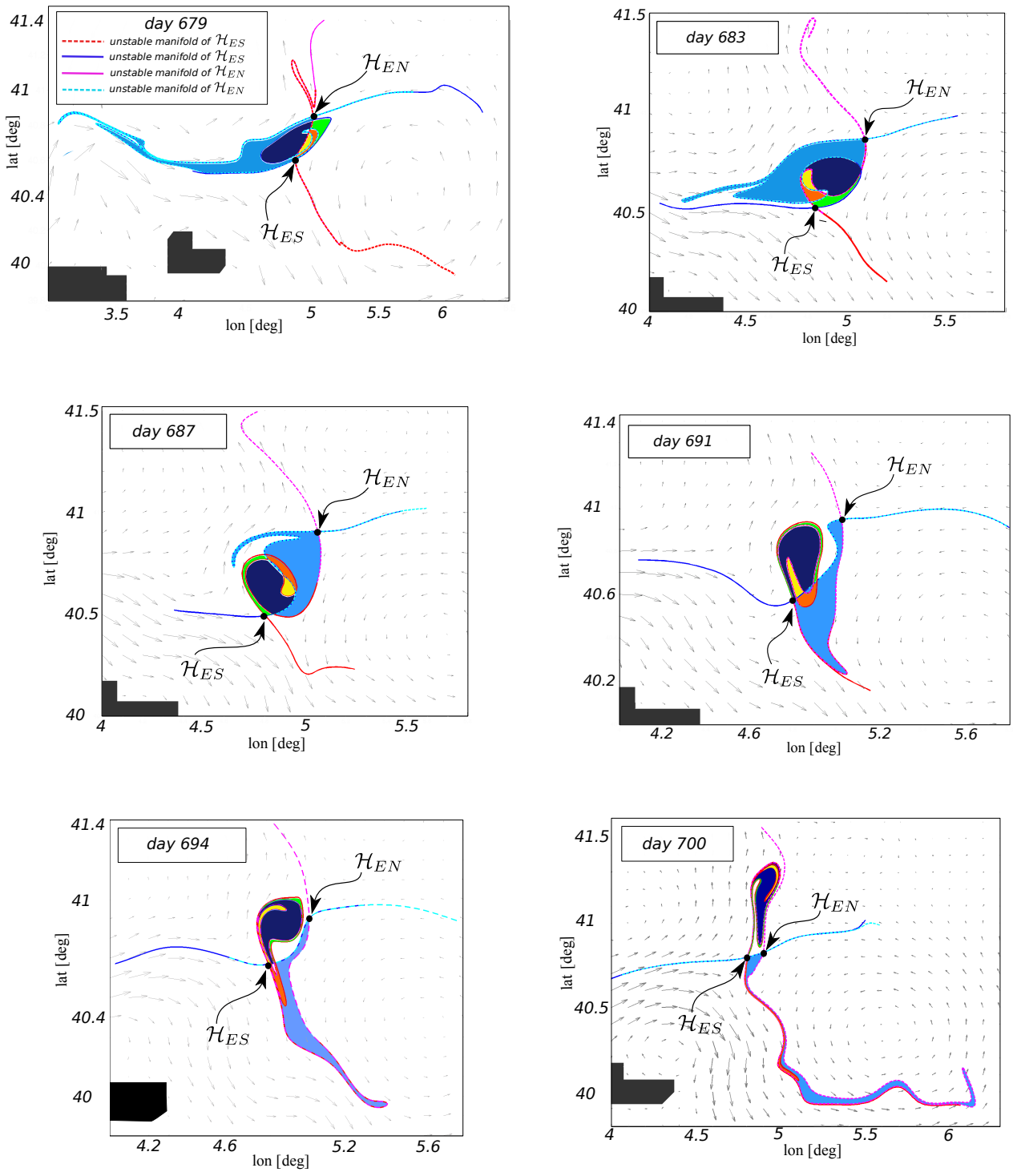

Figure 12: **DieCAST model, NW Mediterranean.** Entrainment of water (light blue lobe) from the region north of the front (R_I in figures 4, 10) into the large eddy (R_{III} in figures 4, 10) via the small eddy (R_{IV} in figure 10). Note that this transport route is only possible when the small eddy, created when the two DHTs $\mathcal{H}_{NE}$ and $\mathcal{H}_{NE}$ separate, exists long enough (see figure 17 for the geometry of the DHTs during this process).

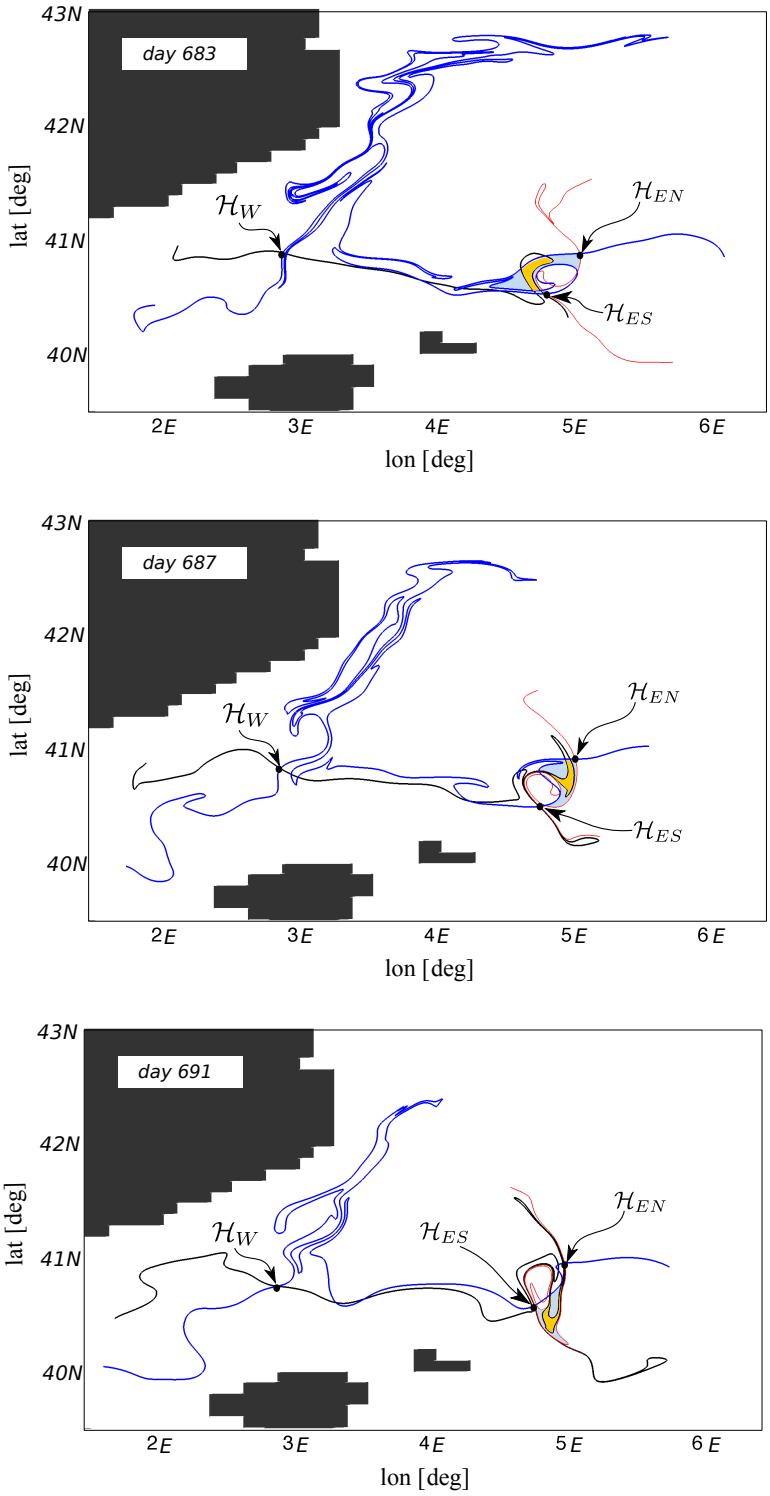

Figure 13: **DieCAST model, NW Mediterranean.** Interaction of a front lobe with a small eddy lobe, revealing a transport route ($R_{II} \to R_I \to R_{IV} \to R_{III}$; see also figure 14b) which is possible only when the flow evolves according to Scenario II for sufficiently long time. This route allows injection of a portion of hot southern waters which crossed the front inside a front lobe (shaded) into the large eddy region across the small eddy region R_{IV}.

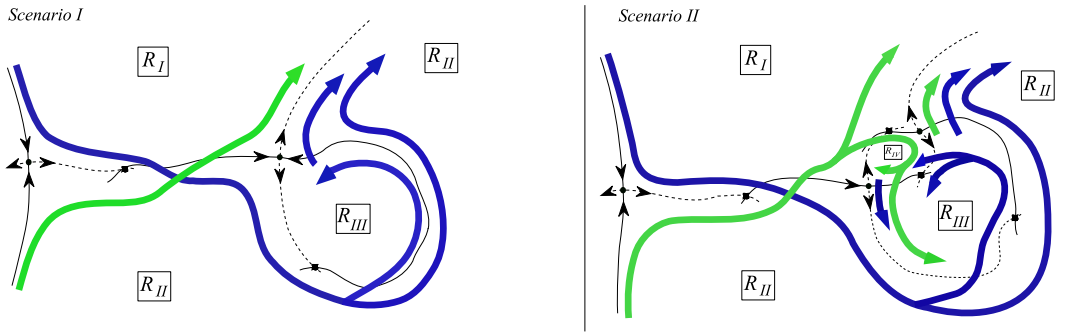

Figure 14: Possible transport routes for front lobes which originate near the stable manifold of $\mathcal{H}_W$ in the far North (blue) or in the far South (green) at $t \to -\infty$. Note that these transport routes may be terminated prematurely if the Lagrangian geometry of the underlying flow evolves into one different than those of Scenario I and II. Note also that the journey of the southern lobes indicated in Scenario II by the green branch: $R_{II} \to R_I \to R_{IV} \to R_{III}$ may be severely affected if the flow does not remain in the Lagrangian configuration of Scenario II for a sufficiently long time.

not allow for such a process to take place. A proper description of transport processes in such a case would therefore require considering the geometry of all intersecting invariant manifolds of an extended system, including the stable and unstable manifolds associated with the additional Lagrangian flow structure which interacts with the front-eddy system.

4.3 Time transition between Scenario I and Scenario II

The studied example of the flow in the North-Western Mediterranean Sea shows an intermittent evolution between the flow structures of Scenario I and II. The transition between these two flow configurations is usually highlighted by an (Eulerian) bifurcation of the ISPs (cf. Appendix A.1) in the flow, leading to the appearance or disappearance of the second smaller eddy. We managed to understand the Lagrangian transport mechanisms associated with each of these scenarios by uncovering the structure of intersecting stable and unstable manifolds of the relevant DHTs in the flow within conveniently chosen time intervals. Recall that we identified two such DHTs ($\mathcal{H}_W$ and $\mathcal{H}_E$), together with their stable and unstable manifolds, in order to describe the geometry of the front interacting with the Lagrangian eddy in Scenario I (see figure 4). In the Lagrangian description of Scenario II we considered three DHTs ($\mathcal{H}_W$, $\mathcal{H}_{SW}$ and $\mathcal{H}_{NE}$) and their invariant manifolds in order to define the front interacting with two Lagrangian eddies (see figure 10). Clearly, in order to understand how the manifold tangle associated with the two DHTs of Scenario I can evolve into the manifold tangle of three DHTs in Scenario II, we first need to understand the relationship between the two sets of DHTs throughout the time interval corresponding to the transition. Then, we can understand the effect of such a transition on the Lagrangian transport in the underlying flow by analysing the evolution of the relevant invariant manifolds. Lagrangian descriptions of flow transitions of this type have received little attention in the geophysical fluid dynamics literature and there is no rigorous mathematical theory to guide our analysis.

In order to isolate the relevant geometrical structures and behaviour in a controlled setting we first consider a kinematic model of the local flow in the front-eddy system in the neighbourhood of the bifurcating ISPs, given by the streamfunction

$$\psi = -s(t)xy + (v(t)/2\delta)e^{-\delta(x^2+y^2)} + \beta(y-x), \qquad s, v, \delta, \beta \geqslant 0 \tag{5}$$

where the first term represents the linear, time-dependent strain, the second term represents

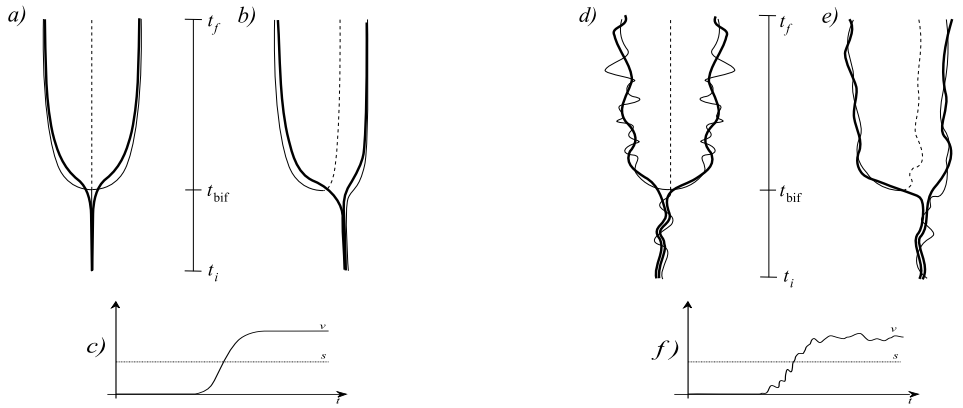

Figure 15: Sketches of projections of the ISP's (thin) and the DHT's (thick) onto the plane $(x, y, t) = (x, -x, t)$ in the extended phase space of the system (6), corresponding to two unfoldings of the normal form for the pitchfork bifurcation (7). a,b,c) the asymptotically steady evolution of (6) and d,e,f) an arbitrary time dependence.

a time-dependent vortex flow, and the last term represents a uniform flow. The choice of the amplitude functions $s(t)$ and $v(t)$ will determine a particular scenario; it will soon become clear that the amplitude of the uniform flow β represents a symmetry breaking parameter when considering bifurcations of the ISPs present in the flow.

The velocity field corresponding to (5) is given by:

$$\left.\begin{aligned} \dot{x} &= -s(t)x - v(t)e^{-\delta(x^2+y^2)}y + \beta \\ \dot{y} &= \ \ s(t)y + v(t)e^{-\delta(x^2+y^2)}x + \beta \end{aligned}\right\} \tag{6}$$

It is straightforward to determine that the ISPs in such a flow must lie on the line $y = -x$ and that, assuming $x, y \ll 1$, their location on this line in terms of distance from the origin, $\varrho = (x^2 + y(x)^2)^{1/2}$, is given by the roots of

$$F(\varrho) = (v - s)\varrho - v\varrho^3 + \beta + \mathcal{O}(\varrho^5). \tag{7}$$

The first two terms in (7) can be recognised as the normal form of a pitchfork bifurcation. We note that in our setting the bifurcation parameter, $\lambda = v(t) - s(t)$, is actually a function of time; β is in this case one of the unfolding parameters of this normal form into a corresponding non-degenerate, third-order form $\tilde{F} = (v - s)\varrho + v\varrho^3 + \alpha\varrho^2 + \beta$. Provided the bifurcation parameter λ increases monotonically in time ($\dot{\lambda} > 0$) there is one hyperbolic ISP in the system before the bifurcation takes place at, say $t_{\rm bif}$, and there are three ISPs (one elliptic and two hyperbolic) after the bifurcation.

In figure 15 we illustrate two different possible bifurcations of the ISPs which can be obtained in system (6) from the unfolding of (7) for different values of β. The sketches shown in figures 15a,b correspond to an asymptotically steady evolution of (6) when $\lambda(t)$ has the form of a sigmoid (figure 15c). The sketches shown in figures 15c,d illustrate the same two types of bifurcations as in figures 15a,b but with λ varying in time in a more complicated fashion. In the symmetric case, when $\beta = 0$ (codimension-two bifurcation), the original ISP bifurcates into three new ISPs in a familiar pitchfork bifurcation (figure 15a,d), which occurs at $t_{\rm bif}$ such that $v(t_{\rm bif}) = s(t_{\rm bif})$. When $\beta \neq 0$, two new ISPs, one elliptic and and one hyperbolic, are born in a saddle-node bifurcation and exist, for $t > t_{\rm bif}$, alongside the original ISP (figure 15b,e).

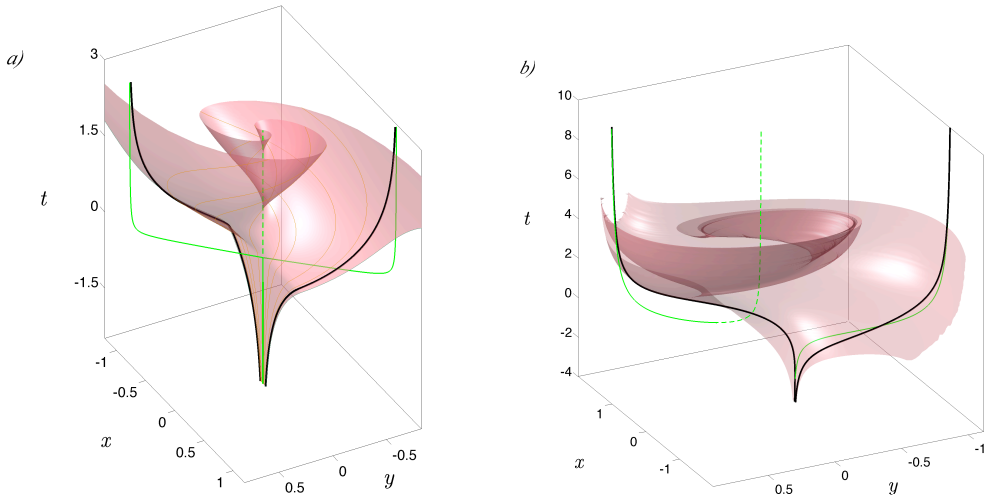

Figure 16: Geometry of the DHTs (black) and their unstable manifolds (red) computed for the system (6) in the asymptotically steady case when: a) the symmetric pitchfork bifurcation ($\beta = 0$) of the system's ISPs (green) takes place; b) the saddle-node bifurcation of the system's ISPs occurs ($\beta \neq 0$).

Consider now the system (6) on the time-interval, $\mathcal{T} = [t_i,\ t_f]$, containing the bifurcation time of the ISPs (i.e. $t_{\text{bif}} \in \mathcal{T}$) so that the flow evolution corresponds locally to the transition between Scenarios I and II. We study first an asymptotically steady evolution of (6) by setting set $s = 1$ and $v = \text{atan}(5\,t) - \text{atan}(5\,t_i)$ (cf. figure 15c). This represents a flow evolving from a pure strain, characterised by a single hyperbolic ISP, to the familiar cat's-eye flow, having two hyperbolic ISPs. The advantage of considering such a time dependence lies in the fact that, if we allow $\mathcal{T} = I\!R$, the DHTs present in the flow must necessarily converge to the hyperbolic ISPs of (6) for $t \to \pm\infty$, since these ISPs are the only bounded, hyperbolic trajectories in the steady flow limit.

If there is a symmetric pitchfork bifurcation in the flow (6) (i.e. when $\beta = 0$), the two continuous paths of hyperbolic ISPs which exist throughout the time interval $\mathcal{T}$ can be used as the initial guesses in the DHT-finding algorithm [23]. Results of this procedure are presented in figure 16a where the computed DHTs are shown as black curves in the extended phase space of the system (spanned by the two spatial directions and time). The red surface also shown there is obtained by recording the time-evolution of the unstable manifolds of the two DHTs in the extended phase space. These two (finite-length) manifold segments are so close tho each other that they are virtually indistinguishable numerically. Note that as the DHTs diverge from each other, parts of their unstable manifolds are rolled up around the (red-coloured) trajectory which coincides with the bifurcated elliptic ISP, indicating the the centre of an eulerian eddy. In order to identify the boundary of the Lagrangian eddy, defined earlier in Appendix A, we would also have to show the geometry of the stable manifolds of the two DHTs, which we avoid for visual clarity. The computed DHTs approach each other for $t < t_{\text{bif}}$, when following them backward in time, and they become virtually indistinguishable when $t \to -\infty$ (not shown in figure 16). It can also be seen that for $t \to t_i$ or $t \to t_f$, when the system (6) is effectively time-independent due to our choice of the amplitudes, $v(t)$ and $s(t)$, the two DHTs converge towards the paths of ISPs, as expected.

When the system (6) undergoes the saddle-node bifurcation of the ISPs (i.e. when $\beta \neq 0$), the problem of computing the DHTs in the flow becomes more cumbersome. In such a case we only have one path of ISPs which stretches across the whole time interval $\mathcal{T}$. Consequently, we

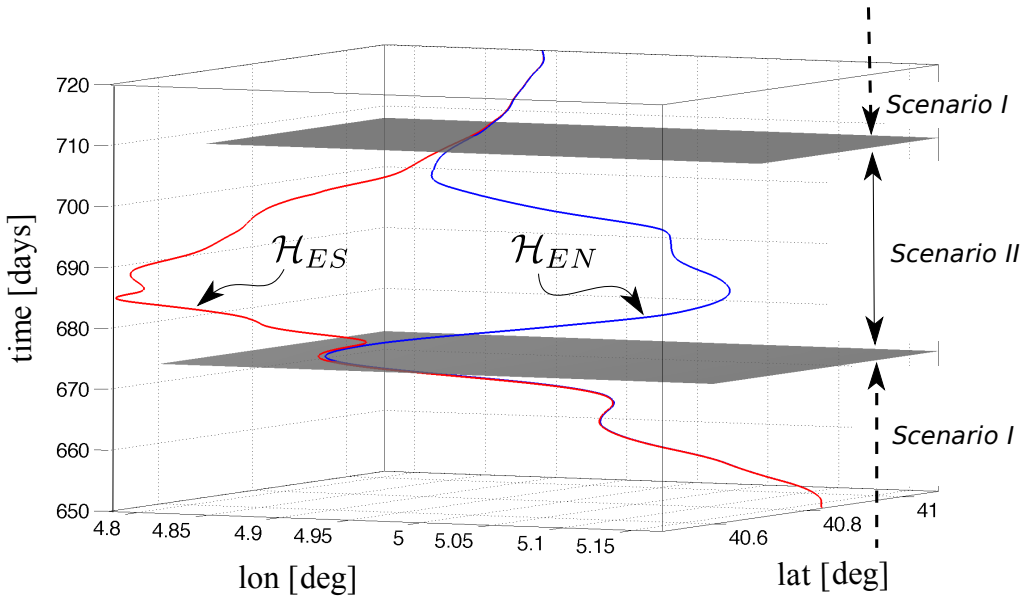

Figure 17: **DieCAST model**. Geometry of the two DHTs, $\mathcal{H}_{NE}$ and $\mathcal{H}_{NE}$, involved in the transition between Scenario I and Scenario II. Note that these DHTs only diverge from each other when Scenario II operates in the flow.

have only one 'good' guess which allows us to find, using the iterative DHT-finding algorithm, the location of only one of the two the DHTs which we expect to be present in the flow, at least in the asymptotically steady case. However, based on the geometry described for the symmetric case and the fact that for $\beta \ll 1$ the saddle-node bifurcation of the ISPs takes place close to the original path of ISPs (see (7)), we can attempt to construct a continuously differentiable (hyperbolic) guess for the second DHT by extending the bifurcated hyperbolic path of ISPs backward in time in such a way that it approaches the first DHT (in a time-backward sense) when $t_{\text{bif}} - t \gg 1$. This heuristic method proves very useful in locating the second DHT for the class of problems we consider (we do not, as yet, have more rigorous estimates on the range of situations for which such a method is successful).

In figure 16b we show the results of computations performed in the system (6) having the same time dependence as that used in figure 16a but undergoing the saddle node bifurcation of the ISPs (i.e. $\beta \neq 0$). The DHTs identified in the flow are shown as the thick black curves. The paths of the hyperbolic ISP are shown in green and the path of the elliptic ISP is shown in red. It is again remarkable that the computed segments of unstable manifolds of the two DHTs seem to coincide throughout the whole time interval $\mathcal{T}$. The surface corresponding to the time evolution of the unstable manifold of one of the DHTs is shown in olive-green and the surface for the other DHTs is numerically indistinguishable from the one shown. The asymptotic steady streamline pattern is again the 'cat's eye' pattern even though the Eulerian characteristics of the transition to this configuration, i.e. the bifurcation of the ISPs, was rather different.

Finally, figure 17 shows results of applying the procedure for identifying the DHTs and their manifolds during the transition between Scenario I and II in a flow generated by the

DieCAST model. Clearly, a similar trajectory geometry to that of figure 16 is revealed. These DHTs were used in manifold computations shown earlier in figure 12 (and also figures 6, 7,13).

Based on the above examples and the results shown in figure 12, three important conclusions can be drawn:

1) It can be clearly seen there that the two computed, finite-length segments of the stable manifolds are very close to each other at all times in the region corresponding to the large eddy away from the small eddy (cf. figures 4, 10). This implies that, even though the boundary of the large eddy could be considered as having a fine structure, associated with the tightly packed segments of the two stable manifolds, $W^u_{\mathcal{H}_{ES}}$ and $W^u_{\mathcal{H}_{EN}}$, any lobes that could be formed by the intersections of this structure with the unstable manifolds would have a negligible area and would not therefore affect the Lagrangian transport across the corresponding boundary.

2) The manifold structure associated with Scenario I can be regarded as being made up of two almost identical copies of manifolds: one associated with $\mathcal{H}_{ES}$ and the other associated with $\mathcal{H}_{EN}$. Since these two structures, including the DHTs, are practically indistinguishable during the operation of Scenario I, we can identify the DHT labelled $\mathcal{H}_E$ in the description of Scenario I with any of the two DHTs, $\mathcal{H}_{ES}$ or $\mathcal{H}_{EN}$, associated with the small eddy in Scenario II.

3) During the transition from Scenario I to Scenario II, the two stable manifolds separate only in the neighbourhood of the two DHTs with which they are associated. This allows one to identify the boundary of the small Lagrangian eddy formed by segments of the unstable manifolds intersecting independently $W^s_{\mathcal{H}_{ES}}$ and $W^s_{\mathcal{H}_{EN}}$. Thus, although both these DHTs exist within the time interval when the flow evolves according to Scenario I, we only need to consider one DHT (labeled $\mathcal{H}_E$ in Scenario I).

In summary, from the analysis of the kinematic model we have learned the following which appear to be the essential geometrical and kinematical features of the flow that are involved in the structural transition of the flow from Scenario I to Scenario II that is associated with the birth of a satellite eddy near the Eastern DHT ($\mathcal{H}_E$) recognised in Scenario I (§4.1). The emergence of the satellite eddy requires the presence of an additional DHT in the flow which remains very close the $\mathcal{H}_E$ during the time interval associated with flow evolution described by Scenario I. (The additional DHT is denoted as $\mathcal{H}_{NE}$ in the description of Scenario II, discussed in §4.2, and $\mathcal{H}_E$ from Scenario I is equivalent to $\mathcal{H}_{SW}$ in Scenario II.) Moreover, the stable and unstable manifolds of these two DHTs, or at least the finite-length segments of the computed manifolds, also remain very close to each other before the transition. During the birth of the second eddy, the DHTs diverge from each other along the unstable manifold of $\mathcal{H}_E$ so that their unstable manifolds are 'shadowing' each other even after the transition (figure 16). The stable manifolds of the two DHTs, denoted as $\mathcal{H}_{SW}$ and $\mathcal{H}_{NE}$ according to the nomenclature of Scenario II, do not coincide after the transition and their transverse intersections with the unstable manifolds can be used to determine the boundary of the second eddy (figures 10, 11).

5 Conclusions

In this paper we have continued the study started in [30] of Lagrangian transport near the North Balearic Front in the Northwestern Mediterranean Sea using the velocity field obtained from the numerical model DieCAST. As in the previous work, the problem is approached from the point of view of dynamical systems theory. We focussed on transport associated with the interaction of the front with one, or two eddies. The numerical simulation provides

us with an Eulerian view of the flow and we use the dynamical systems approach to identify relevant hyperbolic trajectories and their stable and unstable manifolds which are used to uncover a Lagrangian structure of the front-eddy system. The Eulerian framework is insufficient for understanding transport properties in such complicated flows. We showed that Lagrangian transport in the system is effected by the turnstile mechanism whose temporal evolution reveals the spatio-temporal routes along which transport occurs. We also showed that different transport routes are possible depending on whether the front interacts with one or two eddies. We provided the Lagrangian characterization of eddies and presented detailed studies of their transport properties in a 'realistic oceanographic data set'. Also, the 'Lagrangian interaction' of eddies with a front was discussed and analysed. Our work is the first of this type in an oceanographic context. Moreover, we considered the transport implications associated with the transition between the one and two eddy situation and showed how some transport routes can be activated or deactivated due to the transition. We expect that this type of transition between different Eulerian flow structures is common in geophysical flows and that it will involve a variety of different Lagrangian scenarios beyond those studied in this paper. We introduced a local kinematic model which provided insights into the nature of the change in hyperbolic trajectories and their stable and unstable manifolds associated with the "birth and death" of eddies. Further mathematical development from such insights will be crucial for understanding the implications for Lagrangian transport in much more complicated front-eddy systems than those identified in our particular data set.

Acknowledgements

A.M.M. acknowledges the financial support from grants CSIC-OCEANTECH, I-Math C3-0104, MICINN MTM2008-03754 and MTM2008-03840-E; M. B. and S. W. acknowledge financial support from ONR Grant No. N00014-01-1-0769. We also acknowledge Vicente Fernández for providing us with data from the DieCAST simulations.

A The Basic "building blocks" from dynamical systems theory for analyzing Lagrangian transport

Recall that the Eulerian flow features we identify in the data obtained from the DieCAST ocean model can be regarded as two-dimensional to a good approximation during the time interval considered (about 20 days; see §2). We thus recall the most important notions used to develop the Lagrangian characterisation of these features in their two-dimensional formulation. However, most of these tools can be generalised and applied to three-dimensional flows.

First we describe the "Eulerian notion" of an instantaneous stagnation point. While these are (generally) not fluid particle trajectories, they may be useful "signatures" associated with Eulerian structures which suggest a need for a Lagrangian transport analysis.

A.1 Hyperbolic instantaneous stagnation points (ISP's)

Consider a dynamical system, associated with a two-dimensional velocity field $\boldsymbol{v}$ over a time interval $\mathcal{T}$, given by

$$\dot{\boldsymbol{x}} = \boldsymbol{v}(\boldsymbol{x}, t), \quad \boldsymbol{x} \in \mathscr{D}, \quad t \in [t_i,\ t_f] \equiv \mathcal{T}, \tag{8}$$

where $\mathscr{D} \subset I\!R^2$ is the domain of $\boldsymbol{v}$. We explicitly assume that the system (8) is defined over a finite-time interval (i.e. $t_i, > -\infty$, $t_f < \infty$) which has important consequences in further considerations.

An *instantaneous stagnation point*, $\boldsymbol{x}_{isp}$ satisfies $\boldsymbol{v}(\boldsymbol{x}_{isp}, t^*) = 0$ for some $t^* \in \mathcal{T}$. We say that an ISP is (frozen-time) hyperbolic if the Jacobian matrix of the linearization about $\boldsymbol{x}^*$ at a fixed time t^*, i.e. $\partial \boldsymbol{v}(\boldsymbol{x}, t^*)/\partial \boldsymbol{x}|_{\boldsymbol{x}=\boldsymbol{x}^*}$, has two real, non-zero eigenvalues. (For 2D, incompressible flows this reduces to a requirement that the eigenvalues are of equal magnitudes but opposite signs). If the eigenvalues are pure imaginary and complex conjugates of each other, we say that the corresponding ISP is (frozen-time) elliptic. It turns out that, for as long as the ISP remains hyperbolic, one can continue a unique curve of ISPs in time (i.e. a path of ISPs in the extended phase space (x, y, t)), which is given implicitly by

$$\boldsymbol{v}(\boldsymbol{x}_{\rm isp}(t), t) = 0, \qquad t \in \tilde{\mathcal{T}}, \tag{9}$$

where $\tilde{\mathcal{T}} \subset \mathcal{T}$ is a time interval within which the Jacobian, $\left|\partial \boldsymbol{v}(\boldsymbol{x}, t)/\partial \boldsymbol{x}|_{\boldsymbol{x}=\boldsymbol{x}_{\rm isp}(t)}\right|$, does not vanish, as required by the Implicit Function Theorem (see [32] for more information and further references). It is often the case that the Jacobian of the (frozen-time) linearisation about a hyperbolic ISP vanishes at some time, say $t = \tilde{t}$, as the path of ISPs is continued either forward or backward in time. Such points correspond to bifurcations of ISPs and are, in some special cases, associated with changes in the Lagrangian structure of the flow (see, for example, §4.3 below). There is no general relationship between the (Eulerian) structure of ISPs in the time-dependent velocity field $\boldsymbol{v}$ and the Lagrangian structure of trajectories of the corresponding dynamical system (8). The paths of ISPs do not generally correspond to trajectories of the system (8) and they can often be eliminated by an appropriate coordinate transformation. Similarly, the instantaneous streamline patterns do not coincide with any invariant structures in the flow and attempts to determine transport properties from their geometry are generally inappropriate (unless the flow is steady or slowly varying). However, the paths of hyperbolic ISPs can be used as an initial guess in an iterative algorithm developed in [23] which identifies a class of *hyperbolic trajectories* of the system (8) which are important in transport considerations.

A.2 Finite-time, Distinguished Hyperbolic Trajectories (DHTs)

Let $\boldsymbol{x} = \boldsymbol{\gamma}(t)$ be a trajectory of the system (8) and consider a linearisation of the flow about $\boldsymbol{\gamma}$ [5] in the form

$$\dot{\boldsymbol{\xi}} = \partial_{\boldsymbol{x}} \boldsymbol{v}(\boldsymbol{\gamma}(t), t)\, \boldsymbol{\xi}, \tag{10}$$

where $\boldsymbol{\xi} = \boldsymbol{x} - \boldsymbol{\gamma}$ and $\partial_{\boldsymbol{x}} \boldsymbol{v}(\boldsymbol{\gamma}(t), t)$ is the Jacobian of $\boldsymbol{v}(\boldsymbol{x}, t)$ evaluated at $\boldsymbol{x} = \boldsymbol{\gamma}(t)$.

We say that $\boldsymbol{\gamma}(t)$ is finite-time hyperbolic on the time interval $\mathcal{T} = [t_i,\ t_f]$ if the equation (10) has an *exponential dichotomy* on $\mathcal{T}$. Roughly speaking, this means that trajectories located sufficiently close to $\boldsymbol{\gamma}$ can separate at an exponential rate. Formally, the equation (10) has the exponential dichotomy on $\mathcal{T}$ if there exists a projection $\mathbf{P}$ ($\mathbf{P^2} = \mathbf{P}$), and positive constants K, L, α, and β such that:

$$\begin{aligned} |\mathbf{X}(t, t_i)\mathbf{P}\mathbf{X}^{-1}(s, t_i)| &\leqslant K e^{-\alpha(t-s)}, \quad \text{for} \quad t \geqslant s, \quad t, s \in [t_i,\ t_f], \\ |\mathbf{X}(t, t_i)(\mathbf{Id} - \mathbf{P})\mathbf{X}^{-1}(s, t_i)| &\leqslant L e^{-\beta(s-t)}, \quad \text{for} \quad s \geqslant t, \quad t, s \in [t_i,\ t_f], \end{aligned} \tag{11}$$

[5] Dynamical systems theory can often suffer from a proliferation of notation that may tend to obscure understanding. In our setting hyperbolic trajectories are generally time-dependent, and are denoted by $\boldsymbol{\gamma}$. However, in some cases denoting the specific time dependence is not necessary and for the sake of a less cumbersome notation we may simply denote it as $\boldsymbol{\gamma}$.

where $\mathbf{X}$ is the fundamental solution matrix of the system (10) (see [23, 8, 22, 36] for more information).

Similarly to the infinite-time setting, hyperbolic trajectories in flows defined by (8) over a finite time interval are clustered into highly convoluted, connected sets in the extended phase space $\mathcal{D} \times \mathcal{T}$ of the system (8). When analysing the Lagrangian transport in such flows, it is important to identify the location of those trajectories in the hyperbolic structures which play a 'distinguished' role as their 'organising centres'. We refer to such trajectories as *Distinguished Hyperbolic Trajectories* (DHTs). The notion of what is meant by the term "distinguished" is discussed in more detail in [23, 32, 28].

The DHTs cannot, generally, be found analytically and we use the algorithm developed in [23, 24] to locate them. We emphasise here that, although we often use carefully chosen hyperbolic paths of ISPs of (8) as initial guesses in this iterative procedure, any frozen-time-hyperbolic path in the flow (8) can be used as the input for the algorithm if it leads to its convergence (see [24]). Due to the fact that the flow given by (8) is only known for a finite time interval, no DHT can be determined uniquely (cf. [23]). Instead, there exist a small neighbourhood of hyperbolic trajectories in (x, y, t) which can serve as the distinguished ones. The volume of this neighbourhood shrinks with increasing length of the time interval. In this work our use of the term DHT is utilitarian in the sense that the finite-time hyperbolic trajectories, and their associated stable and unstable manifolds, that we identify are constructed with particle trajectories and they provide a description of the transport associated with the front-eddy system that leads to a precise spatio-temporal description of Lagrangian transport.

A.3 Stable and unstable manifolds of DHTs.

The usefulness of the notion of hyperbolicity in transport considerations comes from the fact that one can define stable and unstable manifolds of a hyperbolic trajectory in time-dependent flows in a way analogous to associating separatrix streamlines with saddle points in steady flows. In the case of flows defined for all time, a *stable manifold* of a hyperbolic trajectory $\boldsymbol{\gamma}$, denoted at the time instant t^* by $W^s_\gamma(t^*)$, is defined as a set of points such that trajectories passing through these points at $t = t^*$ will approach $\boldsymbol{\gamma}$ at an exponential rate as time goes to infinity. (It can be shown that for two dimensional incompressible flows such a set of points lies on a curve.) Consequently, an *unstable manifold* at time t^*, denoted by $W^u_\gamma(t^*)$, corresponds to a curve having the property that trajectories passing through any point on this curve at $t = t^*$ approach $\boldsymbol{\gamma}$ at an exponential rate as time goes to minus infinity.

In the case of flows whose evolution is known only over the time interval $\mathcal{T} = [t_i,\ t_f]$ the above definitions have to be modified. A finite-time stable manifold of the hyperbolic trajectory $\boldsymbol{\gamma}(t)$ contains all trajectories, say $\boldsymbol{x}^s(t)$, whose distance from $\boldsymbol{\gamma}$ is smaller than the initial separation, i.e. $|\boldsymbol{\gamma}(t) - \boldsymbol{x}^s(t)| < |\boldsymbol{\gamma}(t_i) - \boldsymbol{x}^s(t_i)|$ for $t \in (t_i,\ t_f]$. Similarly, a finite-time unstable manifold contains all trajectories $\boldsymbol{x}^u$ whose distance from $\boldsymbol{\gamma}$ is less than the final distance, i.e. $|\boldsymbol{\gamma}(t_f) - \boldsymbol{x}^s(t_f)| < |\boldsymbol{\gamma}(t) - \boldsymbol{x}^s(t)|$ for $t \in [t_i,\ t_f)$. As long as the time interval $\mathcal{T}$ is finite, these manifolds have a non-zero volume in the extended phase space (x, y, t).

The link between the two definitions (i.e. in the finite- or infinite-time setting), is revealed when considering a finite-time evolution of a flow defined for all time. Then, every infinite-time hyperbolic trajectory has the 'true' stable and unstable manifolds which are contained within their 'thick' finite-time counterparts. Moreover, all the material manifolds (i.e. manifolds composed of the flow trajectories) contained in the finite-time unstable manifold identified for $\mathcal{T} = [t_i,\ t_f]$ necessarily approach the 'true' unstable manifold when we consider the flow evolution past t_f. Similarly, all material manifolds contained in the finite-time stable manifold identified for $\mathcal{T} = [t_i,\ t_f]$ necessarily approach the 'true' stable manifold when

considering the backward-time flow evolution past t_i. Of course, this 'asymptotic thinning' is not present for the finite-time stable and unstable manifolds of trajectories which are only finite-time hyperbolic, even in flows defined for all time. In the finite-time setting any material manifold contained, for example, in the finite-time unstable manifold of a DHT can be used in transport considerations. This is because, from the point of view of transport, the 'invariance' property of a chosen material manifold is more important than its uniqueness, as long as this manifold is contained within the finite-time stable or unstable manifolds of the relevant DHT. In our work we compute these manifolds using the algorithms developed in [31, 33] and, when using the notion of the stable (or unstable) manifold, we mean a particular material manifold contained in the corresponding finite-time stable (or unstable) manifold.

A.4 Lobes

Consider a point, $\boldsymbol{p}_i$ which at time $t = t_i$ lies on an intersection of an unstable manifold $W^u_{\gamma_1}(t_i)$ of a hyperbolic trajectory $\boldsymbol{\gamma}_1$, and a stable manifold $W^s_{\gamma_2}(t_i)$ of a hyperbolic trajectory $\boldsymbol{\gamma_2}$ (note that homoclinic intersections are also allowed when $\boldsymbol{\gamma_1} = \boldsymbol{\gamma_2}$, as shown in figure 18). Then, one can construct a path connecting $\boldsymbol{p}_i$ and $\boldsymbol{\gamma_1}(t_i)$ along $W^u_{\gamma_1}(t_i)$, which we denote as $W^u_{\gamma_1}\{\boldsymbol{\gamma}_1(t_i), \boldsymbol{p}_i\}$[6], and another path connecting $\boldsymbol{p}_i$ and $\boldsymbol{\gamma_2}(t_i)$ along $W^s_{\gamma_2}(t_i)$, which we denote as $W^s_{\gamma_2}\{\boldsymbol{\gamma}_2(t_i), \boldsymbol{p}_i\}$. A particular subset of such intersection points, called *primary intersection points* ('pip'), turns out to play an important role in further constructions. Formally a primary intersection point (at the time instant $t = t_i$), of two invariant manifolds of hyperbolic trajectories is defined (see [29]), as a point that satisfies

$$W^u_{\gamma_1}\{\boldsymbol{\gamma}_1(t_i), \boldsymbol{p}_i\} \cap W^s_{\gamma_2}\{\boldsymbol{\gamma}_2(t_i), \boldsymbol{p}_i\} = \boldsymbol{p}_i, \tag{12}$$

i.e. it is the only intersection point of the two manifold segments defined above. Note that the invariance of these manifolds under the flow induced by (8) implies invariance of their intersections which must therefore coincide with some trajectories of (8). Thus, if $\boldsymbol{p}_i$ is a pip at $t = t_i$, its image at some later time, say $t = t_j$, must also be a pip given by $\boldsymbol{p}_j = \mathbf{x}(t_j; t_i, \boldsymbol{p}_i)$, where $\mathbf{x}(\cdot\,; t_i, p_i)$ represents a trajectory of (8) passing through p_i at $t = t_i$. These relations can be cast in terms of a flow-induced mapping $\boldsymbol{f}$[7] between points on the same trajectory as (see also figure 18)

$$p_j = \boldsymbol{f}_j(p_i) \equiv \mathbf{x}(t_j; t_i, \boldsymbol{p}_i), \quad p_i = \boldsymbol{f}_i^{-1}(p_j) \equiv \mathbf{x}(t_i; t_j, \boldsymbol{p}_j). \tag{13}$$

Consider now two pips, $\boldsymbol{p}_i$ and $\boldsymbol{k}_i$ at time t_i, such that there are no other pips on the segments of $W^u_{\gamma_1}(t_i)$ and $W^s_{\gamma_2}(t_i)$ that connect $\boldsymbol{k}_i$ and $\boldsymbol{p}_i$. The invariance of these manifolds and their intersection points, $\boldsymbol{k}_i$ and $\boldsymbol{p}_i$, under the action of the flow induced mapping $\boldsymbol{f}$ implies that the region bounded at $t = t_i$ by the segments $W^u_{\gamma_1}\{\boldsymbol{k}_i, \boldsymbol{p}_i\}$ and $W^s_{\gamma_2}\{\boldsymbol{k}_i, \boldsymbol{p}_i\}$ is also invariant under the action of $\boldsymbol{f}$. We define a *lobe* as the area bounded by these manifold segments, and we denote it by $L^{k_i p_i}$ (see figure 18 and also figure 19). If the flow given by (8) is incompressible (i.e. $\nabla \cdot \boldsymbol{v}) = 0$), the flow-induced map $\boldsymbol{f}$ is volume-preserving and the area of the lobe remains constant throughout the evolution. A thorough discussion of *lobe dynamics* can be found in [40], [9], [44], [29]. Examples of applications to oceanographic flows can be found in [37], [39], [46, 47].

[6] The reader should be cautious here. While the notations $W^u_{\gamma_1}(t_i)$ and $W^u_{\gamma_1}\{\boldsymbol{\gamma}_1(t_i), \boldsymbol{p}_i\}$ appear similar here, they mean something quite different. The former denotes the unstable manifold of $\boldsymbol{\gamma}_1(t_i)$ and the latter denotes a finite piece of the unstable manifold of $\boldsymbol{\gamma}_1(t_i)$, starting at $\boldsymbol{\gamma}_1(t_i)$ and ending at $\boldsymbol{p}_i$.

[7] The notation $\boldsymbol{f}$ will serve to denote the mapping from one point to another along trajectories of the flow. A subscript, say i, on $\boldsymbol{f}$ will denote a specific time t_i at which initial points for the flow map are taken.

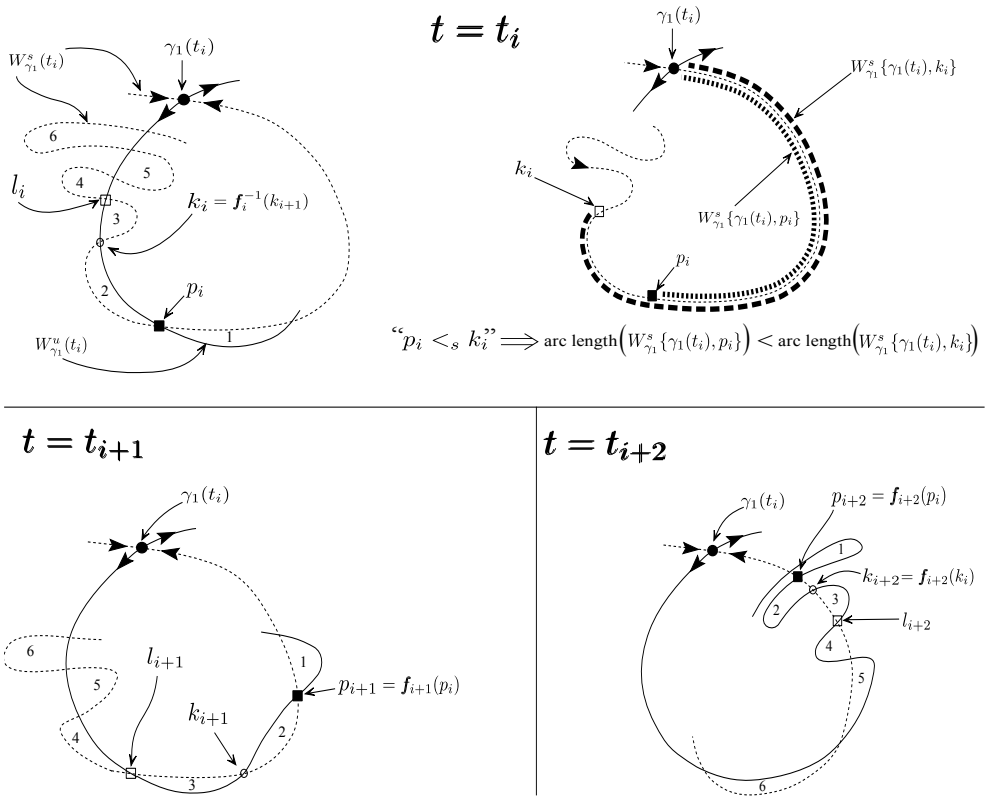

Figure 18: Maintenance of ordering of primary intersection points, $\boldsymbol{p}$ and $\boldsymbol{k}$, under flow evolution illustrated for three different times ($t_i,\ t_{i+1},\ t_{i+2}$). The segment $W^s_{\gamma_1}\{\boldsymbol{\gamma_1(t), p(t)}\}$, connecting $\boldsymbol{\gamma_1}$ and $\boldsymbol{p}(t)$ along the stable manifold of $\boldsymbol{\gamma}_1$, is always shorter than the segment $W^s_{\gamma_1}\{\boldsymbol{\gamma_1(t), k(t)}\}$. The flow induced mapping, $\boldsymbol{f}$ (see (13)), maps the primary intersection points ('pips') along trajectories of the corresponding dynamical system. The evolution of lobes ("1", "2", "3", "4", "5", "6") associated with the boundary $\mathcal{B}(t)$ corresponds to the traditional turnstile mechanism.

A.5 Lagrangian transport associated with lobe dynamics

Given a monotonically increasing sequence of times $\{t_n\}_{n\in\mathbb{Z}}$, and a sequence of pips $\{\boldsymbol{b}_n\}_{n\in\mathbb{Z}}$ along with the corresponding stable and unstable manifold segments (see §A.4), one can construct a family, $\{\mathcal{B}_n\}_{n\in\mathbb{Z}}$, which forms a 'leaky' Lagrangian transport barrier (see §3.1 and figure 3 for an example). *Turnstile lobes*, which mediate transport across such a time-dependent boundary, are constructed by first considering a sequence of pips $\{\boldsymbol{b}_n\}_{n\in\mathbb{Z}}$ which additionally satisfy the *ordering under time evolution* in the form

$$\boldsymbol{b}_{n-1} <_s \boldsymbol{f}_{n-1}^{-1}(\boldsymbol{b}_n). \tag{14}$$

In the case of the single DHT geometry shown in figure 18, the notation of (14) simply means that $\boldsymbol{b}_{n-1}$ is closer to $\boldsymbol{\gamma}_1(t_{n-1})$ along $W^s_{\gamma_1}(t_{n-1})$, than is $\boldsymbol{f}_{n-1}^{-1}(\boldsymbol{b}_n)$ ($\boldsymbol{f}$ is a flow induced map defined in (13)). Then, if there are N ($N \geqslant 0$) pips between endpoints of the segment $W^s_{\gamma_1}\left\{\boldsymbol{f}_{n-1}^{-1}(\boldsymbol{b}_n), \boldsymbol{b}_{n-1}\right\}$, there exist $N+1$ turnstile lobes associated with the boundary segment $\mathcal{B}_{n-1}$ which are delimited by the intersecting segments $W^u_{\gamma_1}\left\{\boldsymbol{f}_{n-1}^{-1}(\boldsymbol{b}_n), \boldsymbol{b}_{n-1}\right\}$ and $W^s_{\gamma_1}\left\{\boldsymbol{f}_{n-1}^{-1}(\boldsymbol{b}_n), \boldsymbol{b}_{n-1}\right\}$. As time evolves to $t = t_n$, such turnstile lobes are mapped under the flow action $\boldsymbol{f}$ to the lobes delimited by the intersecting segments $W^u_{\gamma_1}\left\{\boldsymbol{b}_n, \boldsymbol{f}_n(\boldsymbol{b}_{n-1})\right\}$ and $W^s_{\gamma_1}\left\{\boldsymbol{b}_n, \boldsymbol{f}_n(\boldsymbol{b}_{n-1})\right\}$. Note that in the case of the manifold geometry sketched in figure 18 and

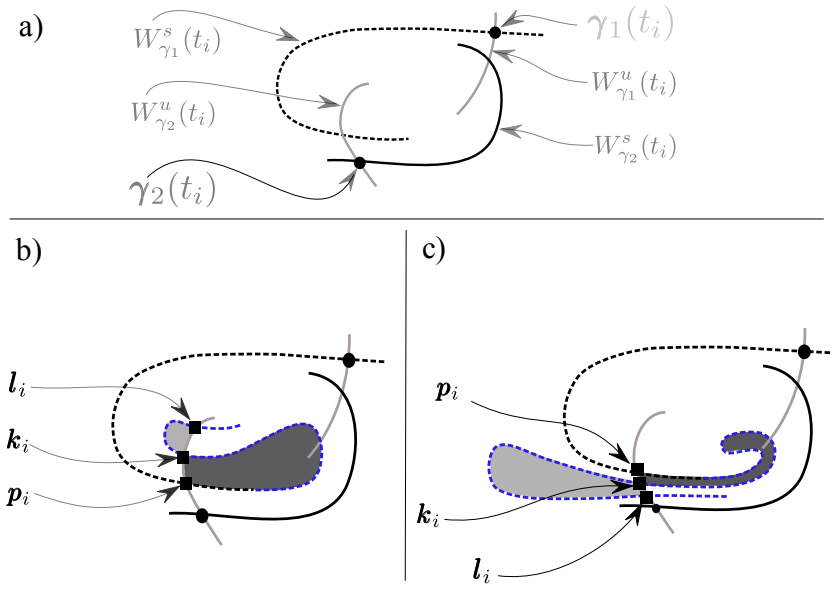

Figure 19: Schematic illustration of instantaneous manifold geometry which generates the same eddy boundary (see (a)) but leads to different transport mechanisms; the two-DHT configuration is used here but the same applies to the single DHT case. b) The ordering of the successive intersection points satisfies $\boldsymbol{p}_i <_{(u,\gamma_2)} \boldsymbol{k}_i <_{(u,\gamma_2)} \boldsymbol{l}_i$ (i.e. $\boldsymbol{p}_i$ is closer to $\boldsymbol{\gamma}_2$ along $W^u_{\gamma_2}$ than $\boldsymbol{k}_i$ and $\boldsymbol{l}_i$). This (invariant) lobe geometry was shown to mediate transport across the small eddy in §4.2 (see also bottom row of figure 3). c) The ordering of successive intersection points satisfies $\boldsymbol{l}_i <_{(u,\gamma_2)} \boldsymbol{k}_i <_{(u,\gamma_2)} \boldsymbol{p}_i$. This traditional turnstile lobe mechanism was shown to operate in the large eddy and across the front (see §4.1 and also figure 18). See §A.5 for more details.

figure 19c, the points $\boldsymbol{p}_i, \boldsymbol{k}_i, \boldsymbol{l}_i$ and their images under the flow induced mapping $\boldsymbol{f}$ can be used as the sequence of pips generating the turnstile lobes. We used this construction extensively in §4.1 and §4.2. If, on the other hand, the manifold geometry is such that $\boldsymbol{p}_i <_u \boldsymbol{k}_i <_u \boldsymbol{l}_i$ these pips and their images under $\boldsymbol{f}$ cannot be used to construct a sequence satisfying (14) (a two-DHT version of such a geometry is shown in figure 19b). The lobes generated in this case are responsible for a new mechanism which was shown to mediate transport through the small eddy in §4.2 (see figure 12).

B Validity of the 2D Lagrangian analysis based on computation of stable and unstable manifolds of hyperbolic trajectories in 3D fluid flows

When applying 2D Lagrangian transport analysis to an output of a 3D numerical ocean model, a natural question arises as to the validity of such an approach. In what follows, we assume that such velocity fields are defined over a finite time interval $I \subset \mathbb{R}$ within a grid of vertically stacked computational levels $L_n \subset \mathbb{R}^2$, $n = 1, 2, \ldots, N$. We determine here conditions under which the knowledge of the time-dependent geometry of stable and unstable manifolds of hyperbolic trajectories computed in a 2D horizontal slice of a 3D fluid flow provides information on Lagrangian transport within a volume of the 3D flow. We argue that structures obtained by a 'vertical extension' of the evolving stable and unstable manifolds are approximately invariant within a layer whose thickness depends on the ratio of the characteristic velocity within the 2D slice to the characteristic vertical shear of the horizontal velocities in the neighbourhood of the considered 2D slice. The smaller the ratio

(in the sense defined below), the thinner the layer within which such 'vertical extensions' of the 2D time-dependent analysis are justified. Conversely, if such a ratio is large the 2D analysis can be valid in a relatively thick layer of the 3D flow. Such time-dependent, vertically extended manifolds do not, in general, coincide with stable and unstable manifolds of hyperbolic trajectories of the full 3D flow. Nevertheless, they represent approximate transport barriers within the corresponding layers.

B.1 Preliminaries

Consider first the following velocity field defined over a finite time interval I

$$\begin{aligned} \boldsymbol{v} &: I\!R^3 \times I \to I\!R^3, \\ \boldsymbol{v}(x,y,z,t) &= \big(u(x,y,t), v(x,y,t), w(x,y,z,t)\big), \end{aligned} \tag{15}$$

where $(x,y,z) \in I\!R^3$, $t \in I \subset I\!R$.

Trajectories of fluid parcels which evolve according to (15), are given by the solutions of

$$\left.\begin{array}{ll} a) & \dot{x} = u(x,y,t) \\ b) & \dot{y} = v(x,y,t) \\ c) & \dot{z} = w(x,y,z,t) \end{array}\right\} \tag{16}$$

Due to the particular functional form of the system (16), (16a-b) can be solved independently of (16c)). Consequently, the solutions of (16) passing through $\boldsymbol{x}_0 = (x_0, y_0, z_0)$ at time $t = t_0$, are given by

$$\boldsymbol{\zeta}(t; \boldsymbol{x}_0, t_0) = \left[\begin{array}{l} \boldsymbol{\zeta}_h\big(t; (x_0, y_0), t_0\big) \\ \zeta_v\big(t; (x_0, y_0, z_0), t_0\big) \end{array}\right], \qquad \boldsymbol{\zeta}(t_0; \boldsymbol{x}_0, t_0) = (\boldsymbol{x}_0, t_0), \tag{17}$$

where

$$\boldsymbol{\zeta} : I \times I\!R^3 \times I \to I\!R^3, \quad \boldsymbol{\zeta}_h : I \times I\!R^2 \times I \to I\!R^2, \qquad \zeta_v : I \times I\!R^3 \times I \to I\!R. \tag{18}$$

Moreover, the solutions (17) of (16) can be embedded in the phase manifold $\mathcal{P} = I\!R^3 \times I$ using a one-parameter family of evolution maps, $\{\phi_\tau\}_{\tau \in I}$, which are defined as

$$\begin{aligned} \phi_\tau &: \mathcal{P} \to \mathcal{P}, \quad \tau \in I, \\ \phi_\tau(\boldsymbol{x}, t) &= \big(\boldsymbol{\zeta}(\tau, \boldsymbol{x}, t), \tau\big), \qquad \phi_t(\boldsymbol{x}, t) = (\boldsymbol{x}, t). \end{aligned} \tag{19}$$

Definition B.1 (*Time slice of the phase manifold) A time slice of $\mathcal{P}$ at time t^* is given by*

$$\mathcal{S}_{t^*} = \{(\boldsymbol{x}, t) \in \mathcal{P} : \quad t = t^*\}. \tag{20}$$

B.2 Invariant manifolds of the system (16)

Consider now a differentiable manifold $\mathcal{M}$ embedded in $\mathcal{P}$ so that any point $\mathfrak{m} \in \mathcal{M}$ can be represented by $(\boldsymbol{x}_\mathfrak{m}, t_\mathfrak{m}) \in \mathcal{P}$. The intersection of $\mathcal{M}$ with $\mathcal{S}_{t^*}$ (i.e. the instantaneous geometry of $\mathcal{M}$) can be represented in $I\!R^3$ as

$$\mathcal{M}_{t^*} = \mathfrak{P}(\mathcal{M} \cap \mathcal{S}_{t^*}), \tag{21}$$

where the injective map $\mathfrak{P}$ is defined as

$$\begin{aligned} \mathfrak{P} &: \mathcal{P} \to I\!R^3, \\ &(\boldsymbol{x}, t) \mapsto \boldsymbol{x}. \end{aligned} \tag{22}$$

Hereafter, we will refer to $\mathcal{M}_{t^*}$ as the *manifold snapshot* at time t^*.

Definition B.2 (*Invariant manifold) We say that a manifold $\mathcal{M} \hookrightarrow \mathcal{P}$ is invariant under the evolution of the dynamical system $\big(\mathcal{P}, \{\phi_\tau\}_{\tau\in I}\big)$ associated with (16) if*

$$\mathfrak{P}\big(\phi_\tau(\mathcal{M}_\kappa, \kappa)\big) = \mathcal{M}_\tau, \tag{23}$$

for every $s, \tau \in I$.

Consider now a time-ordered family of C^r ($r \geqslant 1$) curves

$$\boldsymbol{\gamma}_t : I\!R \to I\!R^2, \quad t \in I, \tag{24}$$

$$s \mapsto \boldsymbol{\gamma}_t(s), \tag{25}$$

representing snapshots of an invariant manifold $\boldsymbol{\gamma} \hookrightarrow I\!R^2 \times I$ of the 2D system (16a-b) ($\boldsymbol{\gamma}_t$ denotes a curve at t parametrised by s). Similarly to (B.2), the invariance of $\boldsymbol{\gamma}$ with respect to the family of maps $\{\varphi_\tau\}_{\tau\in I}$ given by

$$\begin{aligned} &\varphi_\tau : I\!R^2 \times I \to I\!R^2 \times I, \\ &\varphi_\tau(x, y, t) = \big(\boldsymbol{\zeta}_h(\tau, (x, y), t), \tau\big), \end{aligned} \tag{26}$$

implies that

$$\mathfrak{P}_{2D}\big(\varphi_\tau(\boldsymbol{\gamma_\kappa}, \kappa)\big) = \boldsymbol{\gamma_\tau}, \tag{27}$$

where

$$\begin{aligned} \mathfrak{P}_{2D} &: \mathcal{P}_{2D} \to I\!R^2, \\ &(x, y, t) \mapsto (x, y). \end{aligned} \tag{28}$$

We now show that, a manifold $\mathcal{M} \hookrightarrow \mathcal{P}$ whose 2D snapshots are given by

$$\mathcal{M}_t = \boldsymbol{\gamma}_t \times I\!R, \tag{29}$$

is invariant under the evolution induced by (16). In order to prove this, it is sufficient to show that any vertical line, given by

$$\Gamma_{t_1} = \big\{(x, y, z) \in I\!R^3 : \ \ (x, y) = \boldsymbol{\gamma}_{t_1}(s),\ z \in I\!R\big\}, \tag{30}$$

where $t = t_1$ and s are fixed, is mapped into a vertical line at time $t = t_2$ under the evolution of ϕ_{t_2}. This can be checked by explicitly evaluating $\mathfrak{P}\big(\phi_{t_2}(\cdot, t_1)\big)$ at two arbitrary points of Γ_{t_1}, say, $\boldsymbol{p}_i = (\boldsymbol{\gamma}_{t_1}(s), z_i)^T$ and $\boldsymbol{p}_{ii} = (\boldsymbol{\gamma}_{t_1}(s), z_{ii})^T$. These points are mapped at $t = t_2$ to

$$\tilde{\boldsymbol{p}}_i = \mathfrak{P}\big(\phi_{t_2}(\boldsymbol{p}_i, t_1)\big) = \boldsymbol{\zeta}(t_2, \boldsymbol{p}_i, t_1) = \begin{bmatrix} \boldsymbol{\zeta}_h(t_2, \boldsymbol{\gamma}_{t_1}(s), t_1) \\ \zeta_v(t_2, \boldsymbol{p}_i, t_1) \end{bmatrix}, \tag{31}$$

and

$$\tilde{\boldsymbol{p}}_{ii} = \boldsymbol{\mathfrak{P}}\big(\phi_{t_2}(\boldsymbol{p}_{ii}, t_1)\big) = \boldsymbol{\zeta}(t_2, \boldsymbol{p}_{ii}, t_1) = \left[\begin{array}{l} \boldsymbol{\zeta}_h(t_2, \boldsymbol{\gamma}_{t_1}(s), t_1) \\ \zeta_v(t_2, \boldsymbol{p}_{ii}, t_1) \end{array} \right]. \tag{32}$$

Clearly, if $\boldsymbol{p}_i$ and $\boldsymbol{p}_{ii}$ are contained in a vertical line Γ_{t_1}, the points $\tilde{\boldsymbol{p}}_i$ and $\tilde{\boldsymbol{p}}_{ii}$ lie on a vertical line

$$\Gamma_{t_2} = \{(x, y, z) \in I\!R^3 : \ \ (x, y) = \boldsymbol{\zeta}_h(t_2, \boldsymbol{\gamma}_{t_1}(s), t_1), \ z \in I\!R\} \quad (t_1, s \text{ fixed}). \tag{33}$$

The consequences of this fact are two-fold:

(i) One can construct a one-parameter family of 2D manifolds $\{\mathcal{L}^s\}_{s \in I\!R}$ whose snapshots are given by the vertical lines

$$\mathcal{L}^s_t = \boldsymbol{\zeta}_h(t, \boldsymbol{\gamma}_{t_0}(s), t_0) \times I\!R, \tag{34}$$

and such that each $\mathcal{L}^s$ is invariant under the evolution induced by (16) (cf. Definition 2.1) In other words, the vertical line $\mathcal{L}^s_{t_1}$ at $t = t_1$ is mapped under the evolution induced by (15) onto a vertical line $\mathcal{L}^s_{t_2}$ at $t = t_2$. Note that, depending on properties of ζ_v (18), the vertical ordering of points on these lines may change during the evolution.

(ii) Given the ordered sequence of 1D snapshots $\{\boldsymbol{\gamma}_t\}_{t \in I}$ (cf. (24)) representing the invariant manifold of the restricted system (16a-b), the manifold whose snapshots are given by $\mathcal{M}_t = \boldsymbol{\gamma}_t \times I\!R$ is an invariant manifold of the system (16). The 3D invariant manifold $\mathcal{M} \hookrightarrow \mathcal{P}$ is additionally foliated by the 2D invariant manifolds $\mathcal{L}^s \hookrightarrow \mathcal{P}$.

B.2.1 Finite-thickness layer

If the considered layer has a finite thickness

$$\mathfrak{L}_H = \{(x, y, z) \in I\!R^3 : \quad z \in [z_* - H, \ \ z_* + H]\}, \quad 0 < H < \infty, \tag{35}$$

some trajectories of the system (16) contained in the invariant manifolds $\mathcal{L}^s$ (see (34)) may cross the boundary surfaces, $z = z_* - H$ or $z = z_* + H$, during the forward or backward evolution. Note, however, that the determination of the evolving geometry of $\mathcal{M}$ within $\mathfrak{L}_H$ (i.e. $\mathcal{M} \hookrightarrow \mathfrak{L}_H \times I$) does not require the information about the flow beyond $\mathfrak{L}_H$. Consider, for example, a trajectory (3) contained in $\mathcal{L}^s$ in figure 20. Although it cannot be continued within $\mathfrak{L}_H$ beyond $t = t_2$, it can be replaced by another trajectory in the same fibre t_2) since only one trajectory in each fibre is needed to determine the geometry of each $\mathcal{M}_t$.

B.3 General velocity field in Cartesian coordinates

Consider now a situation with an arbitrary (smooth and appropriately non-dimensionalised) velocity field $\boldsymbol{v}(x, y, z, t)$ within a layer, $\mathfrak{L}_H$ (see 35). The dynamical system associated with $\boldsymbol{v}$ is given by

$$\left.\begin{array}{ll} a) & \dot{x} = u(x, y, z, t), \\ b) & \dot{y} = v(x, y, z, t), \\ c) & \dot{z} = w(x, y, z, t), \end{array}\right\} \qquad (x, y, z) \in \mathfrak{L}_H \subset I\!R^3. \tag{36}$$

Consider now this system in the neighbourhood of $z = z_*$, which we can write as

$$\left.\begin{array}{ll} a) & \dot{x} = u(x, y, z_*, t) + hF_u(x, y, h, t), \\ b) & \dot{y} = v(x, y, z_*, t) + hF_v(x, y, h, t), \\ c) & \dot{h} = w(x, y, z_* + h, t), \end{array}\right\}, \qquad (x, y, z_* + h) \in \mathfrak{L}_H, \tag{37}$$

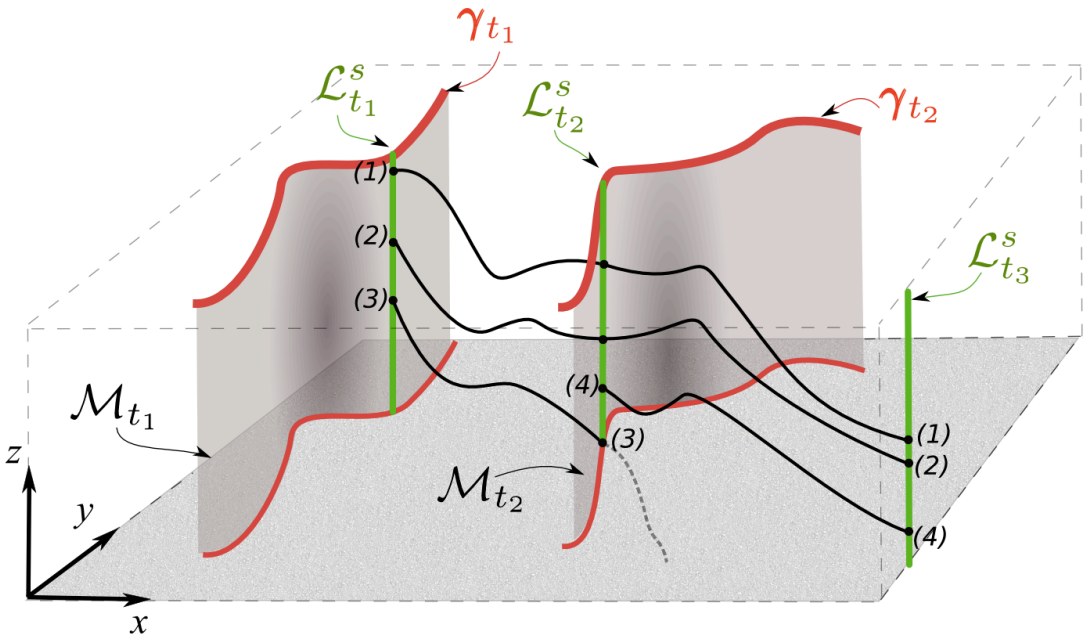

Figure 20: Schematic and simplified illustration of snapshots of an invariant manifold $\mathcal{M}$ obtained by a 'vertical extension' of an invariant manifold $\boldsymbol{\gamma}$ of the reduced system (16a-b) in the phase manifold $\mathcal{P} = I\!R^3 \times I$. Two manifold snapshots in a layer $\mathcal{L}_H \subset I\!R^3$ are shown in grey and the snapshots $\boldsymbol{\gamma}_t$ are shown in red at two different times t_1 and t_2. The corresponding manifold snapshots $\mathcal{M}_t = \{(x,y,z) \in L_n \subset I\!R^3 : \ (x,y) = \boldsymbol{\gamma}_t, \ z \in \mathcal{Z}_n\}$ at two different times are shaded. The invariant manifold $\mathcal{M} \hookrightarrow \mathcal{L}_H \times I$ is fibrated by the family of 2D manifolds $\mathcal{L}^s$ (cf. (34)). Intersections of one such fibre with the snapshots $\mathcal{M}_t$ are given by the green vertical lines. Computation of the manifold snapshots $\mathcal{M}_t$ can be continued beyond the time interval it takes a single trajectory to cross the layer. A trajectory which leaves the layer can be replaced by another trajectory in the fibre (see (3) and (4) at $t = t_2$) since only one trajectory in each fibre is needed to determine the geometry of each $\mathcal{M}_t$.

where

$$F_u(x,y,h,t;z_*) = \frac{\partial u(x,y,z,t)}{\partial z}\Big|_{z=z_*} + \mathcal{O}(h;x,y,t,z_*), \tag{38}$$

$$F_v(x,y,h,t;z_*) = \frac{\partial v(x,y,z,t)}{\partial z}\Big|_{z=z_*} + \mathcal{O}(h;x,y,t;z_*). \tag{39}$$

In (38) and (39), we symbolically represent the higher-order terms in the Taylor expansion about z_* by $\mathcal{O}(h;x,y,t,z_*)$.

We now assume that within $\mathfrak{L}_H$, we have $\epsilon = H/\mathcal{K} \ll 1$ where

$$\mathcal{K} = \min\left[\min_{(x,y,z_*+s)\in\mathfrak{L}_H,\ t\in I}\left[\frac{u(x,y,z_*,t)}{F_u(x,y,s,t)}\right], \min_{(x,y,z_*+s)\in\mathfrak{L}_H,\ t\in I}\left[\frac{v(x,y,z_*,t)}{F_v(x,y,s,t)}\right]\right] \tag{40}$$

In order to highlight this assumption, we introduce ϵ as an ordering parameter in (37) which leads to

$$\left.\begin{array}{ll} a) & \dot{x} = u(x,y,z_*,t) + \epsilon h F_u(x,y,h,t) \\ b) & \dot{y} = v(x,y,z_*,t) + \epsilon h F_v(x,y,h,t) \\ c) & \dot{h} = w(x,y,z_*+h,t) \end{array}\right\}, \qquad (x,y,z_*+h) \in \mathfrak{L}_H. \tag{41}$$

A remark is in order here. Clearly, $\mathcal{K} = 0$ at any ISP (see §A.1) in the flow and the assumption on the smallness of ϵ cannot be valid in a neighbourhood of an ISP (see also figure 21). Analysis of the flow structure in the neighbourhood of such isolated points would require a more involved Melnikov-type treatment, exploiting local analysis of invariant manifold structure in the neighbourhood of such points.

If we now expand x, y and h in the asymptotic series in ϵ, i.e.

$$x = x^{(0)} + \epsilon x^{(1)} + \epsilon^2 x^{(2)} \dots \tag{42}$$

$$y = y^{(0)} + \epsilon y^{(1)} + \epsilon^2 y^{(2)} \dots \tag{43}$$

$$h = h^{(0)} + \epsilon h^{(1)} + \epsilon^2 h^{(2)} \dots, \tag{44}$$

and substitute these into (41) we obtain (upon collecting like terms in powers of ϵ)

$$\epsilon^0 : \left\{ \begin{array}{l} \dot{x}^{(0)} = u(x^{(0)}, y^{(0)}, z_*, t), \\ \dot{y}^{(0)} = v(x^{(0)}, y^{(0)}, z_*, t), \\ \dot{h}^{(0)} = w(x, y, z_* + h^{(0)}, t), \end{array} \right. \tag{45}$$

$$\epsilon^1 : \left\{ \begin{array}{l} \dot{x}^{(1)} = \frac{\partial u(x,y^{(0)},z_*,t)}{\partial x}\big|_{x=x^{(0)}} x^{(1)} + \frac{\partial u(x^{(0)},y,z_*,t)}{\partial y}\big|_{y=y^{(0)}} y^{(1)} + h^{(0)} F_u(x^{(0)}, y^{(0)}, h^{(0)}, t), \\ \dot{y}^{(1)} = \frac{\partial v(x,y^{(0)},z_*,t)}{\partial x}\big|_{x=x^{(0)}} x^{(1)} + \frac{\partial v(x^{(0)},y,z_*,t)}{\partial y}\big|_{y=y^{(0)}} y^{(1)} + h^{(0)} F_v(x^{(0)}, y^{(0)}, h^{(0)}, t), \\ \dot{h}^{(1)} = \frac{\partial w(x,y^{(0)},z_*+h^{(0)},t)}{\partial x}\big|_{x=x^{(0)}} x^{(1)} + \frac{\partial w(x^{(0)},y,z_*+h^{(0)},t)}{\partial y}\big|_{y=y^{(0)}} y^{(1)} + \frac{\partial w(x,y^{(0)},z,t)}{\partial z}\big|_{z=z_*+h^{(0)}} h^{(1)}, \end{array} \right. \tag{46}$$

$$\epsilon^2 : \qquad \dots \tag{47}$$

Note that the leading order solution of (41), corresponding to (45), is given by (17). Consequently, the manifolds $\mathcal{M}_t$, defined in (29), remain invariant with respect to (45). As long as we consider the dynamics within a layer $\mathcal{L}_H$ such that $H \ll \mathcal{K}$, the higher-order solutions contribute to small (order ϵ) perturbations of the 'vertical' invariant structures discussed in §B.2.

B.4 Spherical geometry

Many geophysical models, including DieCast are formulated in spherical coordinates rather than Cartesian coordinates. We briefly outline here the main modifications to the conclusions of the previous sections. Given the velocity field in spherical coordinates, i.e.

$$\boldsymbol{v}(\varphi, \vartheta, r, t) = u_\varphi(\varphi, \vartheta, r, t)\boldsymbol{e}_\varphi + u_\vartheta(\varphi, \vartheta, r, t)\boldsymbol{e}_\vartheta + u_r(\varphi, \vartheta, r, t)\boldsymbol{e}_r \tag{48}$$

within the layer $\mathfrak{L}_H = \{(\varphi, \vartheta, r) \in I\!R^3 : \quad r \in [r_* - H, \;\; r_* + H]\}$, the corresponding dynamical system is given by

$$\left. \begin{array}{ll} a) & \dot{\varphi} = \dfrac{u_\varphi(\varphi, \vartheta, r, t)}{r \sin\vartheta} \\ b) & \dot{\vartheta} = \dfrac{u_\vartheta(\varphi, \vartheta, r, t)}{r} \\ c) & \dot{r} = u_r(\varphi, \vartheta, r, t) \end{array} \right\} \tag{49}$$

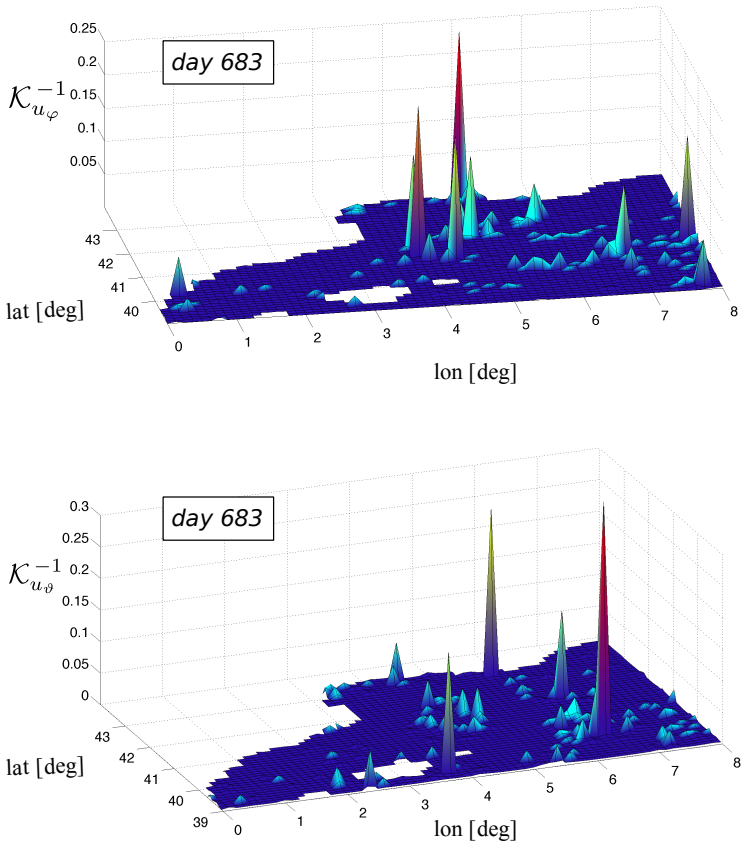

Figure 21: Typical example of the instantaneous values of $\mathcal{K}_{u_\varphi}^{-1}$ and $\mathcal{K}_{u_\vartheta}^{-1}$ which play a role (via (53)) in determining the validity of the 2D analysis of the DieCAST output in the region examined in §4. These values remain small, as desired, except for localised 'spikes' usually associated with the presence of ISPs.

If we consider the dynamics within a layer centered at r_*, the system (49) can be rewritten as

$$\left.\begin{aligned} a)\quad & \dot{\varphi} = \frac{u_\varphi(\varphi,\vartheta,r_*,t)}{r_*\sin\vartheta} + hF_\varphi(\varphi,\vartheta,h,t) \\ b)\quad & \dot{\vartheta} = \frac{u_\vartheta(\varphi,\vartheta,r_*,t)}{r_*} + hF_\vartheta(\varphi,\vartheta,h,t) \\ c)\quad & \dot{h} = u_r(\varphi,\vartheta,r_*+h,t) \end{aligned}\right\} \tag{50}$$

where

$$F_\varphi(\varphi,\vartheta,h,t) = \frac{1}{r_*\sin\vartheta}\left(\frac{\partial u_\varphi(\varphi,\vartheta,r,t)}{\partial r}\Big|_{r=r_*} - \frac{u_\varphi(\varphi,\vartheta,r_*,t)}{r_*\sin\vartheta} + \mathcal{O}(h;\varphi,\vartheta,r_*,t)\right), \tag{51}$$

$$F_\vartheta(\varphi,\vartheta,h,t) = \frac{1}{r_*}\left(\frac{\partial u_\vartheta(\varphi,\vartheta,r,t)}{\partial r}\Big|_{r=r_*} - \frac{u_\vartheta(\varphi,\vartheta,r_*,t)}{r_*} + \mathcal{O}(h;\varphi,\vartheta,r_*,t)\right). \tag{52}$$

Provided that $H \ll \mathcal{K}$ similar conclusions can be drawn as in §B.3 except that $\mathcal{K}$ is given in

this case by

$$\mathcal{K} = \min\left[\min_{(\varphi,\vartheta,r_*+h)\in\mathfrak{L}_H,\ t\in I} \mathcal{K}_{u_\varphi}(\varphi,\vartheta,r_*,t), \min_{(x,y,z_*+s)\in\mathfrak{L}_H,\ t\in I} \mathcal{K}_{u_\vartheta}(\varphi,\vartheta,r_*,t)\right]. \tag{53}$$

where

$$\mathcal{K}_{u_\varphi} = \frac{u_\varphi(\varphi,\vartheta,r_*,t)}{F_\varphi(\varphi,\vartheta,s,t)}, \qquad \mathcal{K}_{u_\vartheta} = \frac{u_\vartheta(\varphi,\vartheta,r_*,t)}{F_\vartheta(\varphi,\vartheta,s,t)}. \tag{54}$$

In figure 21 we show a typical example of the instantaneous fields corresponding to $\mathcal{K}_{u_\varphi}^{-1}$ (figure 21a) and $\mathcal{K}_{u_\vartheta}^{-1}$ (figure 21b) in (53) computed in the layer L_2, centered at 15.93m, where the 2D computations in §4 were performed. The derivatives in $\mathcal{K}_{u_\varphi}$ and $\mathcal{K}_{u_\vartheta}$ were approximated by finite differences between layer L_1 (centred at 5m) and L_2 (centred at 15.93m) and the higher order terms were not considered due to the lack of data on the neighbouring layers (the DieCAST run we had access to stored data at six layers (L_i, $i = 1, 2, 7, 10, 17, 19$) out of the total of 30 computational layers.) Although not shown here, both $\mathcal{K}_{u_\varphi}^{-1}$ and $\mathcal{K}_{u_\vartheta}^{-1}$ remain small except localised and short lived spikes which are usually associated with the ISPs.

References

[1] H. Aref, *The development of chaotic advection*, Phys. Fluids **14(4)** (2002), 1315–1325.

[2] J. H. Bartlett, *Limits of stability for an area-perserving polynomial mapping*, Cel. Mech. **28** (1982), 295–317.

[3] C. Basdevant and T. Philipovitch, *On the validity of the "Weiss criterion" in two-dimensional turbulence*, Physica D **73** (1994), 17–30.

[4] A. S. Bower, *A simple kinematic mechanism for mixing fluid parcels across a meandering jet*, J. Phys. Oceanogr. **21** (1991), 173–180.

[5] M. Cencini, G. Lacorata, A. Vulpiani, and E. Zambianchi, *Mixing in a meandering jet: A Markovian approximation*, J. Phys. Oceanogr. **29(10)** (1999), 2578–2594.

[6] S. R. Channon and J. L. Lebowitz, *Numerical experiments in stochasticity and homoclinic oscillations*, Ann. New York Acad. Sci. **357** (1980), 108–118.

[7] D. B. Chelton, M. G. Schlax, R. M. Samelson, and R. A. de Szoeke, *Global observations of large oceanic eddies*, Geophysical Research Letters **34** (2007), L15606.

[8] W. A. Coppel, *Dichotomies in stability theory*, Lecture Notes in Mathematics, vol. 629, Springer-Verlag, New York, Heidelberg, Berlin, 1978.

[9] C. Coulliette and S. Wiggins, *Intergyre transport in a wind-driven, quasigeostrophic double gyre: An application of lobe dynamics*, Nonlinear Processes in Geophysics **8** (2001), 69–94.

[10] R. Cucitore, M. Quadrio, and A. Baron, *On the effectiveness and limitations of local criteria for the identification of a vortex*, Eur. J. Mech. B/Fluids **18** (1999), no. 2, 261–282.

[11] D. Dietrich, *Application of a modified "a" grid ocean model having reduced numerical dispersion to the Gulf of Mexico circulation*, Dyn. Atmos. Oceans **27** (1997), 201–217.

[12] D. Dietrich, R. Haney, V. Fernández, S. Josey, and J. Tintoré, *Air-sea fluxes based on observed annual cycle surface climatology and ocean model internal dynamics: a non-damping zero-phase-lag approach applied to the Mediterranean sea*, J. Mar. Sys. **52** (2004), 145–165.

[13] J. Q. Duan and S. Wiggins, *Fluid exchange across a meandering jet with quasi-periodic time variability*, J. Phys. Oceanogr. **26** (1996), 1176–1188.

[14] L. H. Duc and S. Siegmund, *Hyperbolicity and invariant manifolds for planar nonautonomous systems on finite time intervals*, Int. J. Bif. Chaos **18** (2008), no. 3, 641–674.

[15] S. Dutkiewicz, A. Griffa, and D. B. Olson, *Particle diffusion in a meandering jet*, J. Geophys. Res. **98(C9)** (1993), 16487–16500.

[16] V. Fernández, D. Dietrich, R. Haney, and J. Tintoré, *Mesoscale, seasonal and interannual variability in the Mediterranean sea using a numerical ocean model*, Progress in Oceanography **66** (2005), 321–340.

[17] G. Haller, *Finding finite-time invariant manifolds in two-dimensional velocity fields*, Chaos **10(1)** (2000), 99–108.

[18] ———, *Lagrangian structures and the rate of strain in a partition of two-dimensional turbulence*, Physics of Fluids **13** (2001), no. 11, 3365–3385.

[19] ———, *Lagrangian coherent structures from approximate velocity data*, Physics of Fluids **14** (2002), no. 6, 1851–1861.

[20] ———, *An objective definition of a vortex*, J. Fluid Mech. **525** (2005), 1–26.

[21] G. Haller and A. Poje, *Finite time transport in aperiodic flows*, Physica D **119** (1998), 352–380.

[22] D. Henry, geometric theory of semilinear parabolic equations, lecture notes in mathematics, vol. 840., Springer-Verlag: New York, Heidelberg, Berlin, 1981.

[23] K. Ide, D. Small, and S. Wiggins, *Distinguished hyperbolic trajectories in time dependent fluid flows: analytical and computational approach for velocity fields defined as data sets*, Nonlinear Processes in Geophysics **9** (2002), 237–263.

[24] N. Ju, D. Small, and S. Wiggins, *Existence and computation of hyperbolic trajectories of aperiodically time-dependent vector fields and their approximations*, Int. J. Bif. Chaos **13** (2003), 1449–1457.

[25] S. Louazel and B. L. Hua, *Vortex erosion in a shallow-water model*, Physics of Fluids **16** (2004), no. 8, 3079–3085.

[26] M. S. Lozier, L. J. Pratt, A. M. Rogerson, and P. D. Miller, *Exchange geometry revealed by float trajectories in the Gulf Stream*, J. Phys. Oceanogr. **27** (1997), 2327–2341.

[27] R. S. MacKay, J. D. Meiss, and I. C. Percival, *Transport in Hamiltonian systems*, Physica D **13** (1984), no. 1-2, 55–81.

[28] J. A. Jiménez Madrid and Ana M. Mancho, *Distinguished trajectories in time dependent vector fields.*, Chaos **19** (2009), 013111–1–013111–18.

[29] N. Malhotra and S. Wiggins, *Geometric structures, lobe dynamics, and Lagrangian transport in flows with aperiodic time-dependence, with applications to Rossby wave flow*, J. Nonlinear Science **8** (1998), 401–456.

[30] A. M. Mancho, E. Hernández-García, D. Small, and S. Wiggins, *Lagrangian transport through an ocean front in the North-Western Mediterranean Sea*, J. Phys. Oceanogr. **??** (2008), ??

[31] A. M. Mancho, D. Small, and S. Wiggins, *Computation of hyperbolic and their stable and unstable manifolds for oceanographic flows represented as data sets*, Nonlinear Processes in Geophysics **11** (2004), 17–33.

[32] ———, *A tutorial on dynamical systems concepts applied to Lagrangian transport in oceanic flows defined as finite time data sets: Theoretical and computational issues*, Physics Reports **437** (2006), 55–124.

[33] A. M. Mancho, D. Small, S. Wiggins, and K. Ide, *Computation of stable and unstable manifolds of hyperbolic trajectories in two-dimensional, aperiodically time-dependent vector fields*, Physica D **182** (2003), 188–222.

[34] S. D. Meyers, *Cross-frontal mixing in a meandering jet*, J. Phys. Oceanogr. **24** (1994), 1641–1646.

[35] P. D. Miller, C. K. R. T. Jones, A. M. Rogerson, and L. J. Pratt, *Quantifying transport in numerically generated velocity fields*, Physica D **110** (1997), 105–122.

[36] J. S. Muldowney, *Dichotomies and asymptotic behaviour for linear differential systems*, Trans. A.M.S. **283(2)** (1984), 465–484.

[37] K. Ngan and T. G. Shepherd, *Chaotic mixing and transport in Rossby wave critical layers*, J. Fluid. Mech. **334** (1997), 315–351.

[38] A. Okubo, *Horizontal dispersion of floatable particles in the vicinity of velocity singularities such as convergences*, Deep-Sea Research **17** (1970), 445–454.

[39] A. M. Rogerson, P. D. Miller, L. J. Pratt, and C. K. R. T. Jones, *Lagrangian motion and fluid exchange in a barotropic meandering jet*, J. Phys. Oceanogr. **29** (1999), 2635–2655.

[40] V. Rom-Kedar, A. Leonard, and S. Wiggins, *An analytical study of transport, mixing, and chaos in an unsteady vortical flow*, J. Fluid Mech. **214** (1990), 347–394.

[41] R. Samelson and S. Wiggins, *Lagrangian transport in geophysical jets and waves: The dynamical systems approach*, Springer-Verlag, New York, 2006.

[42] R. M. Samelson, *Fluid exchange across a meandering jet*, J. Phys. Oceanogr. **22** (1992), 431–440.

[43] Q. Schiermeier, *Churn, churn, churn*, Nature **447** (2007), 522–524.

[44] S. Wiggins, *Chaotic transport in dynamical systems*, Springer-Verlag, New York, 1992.

[45] ———, *The dynamical systems approach to Lagrangian transport in oceanic flows*, Annu. Rev. Fluid Mech. **37** (2005), 295–328.

[46] G.-C. Yuan, L. J. Pratt, and C. K. R. T. Jones, *Barrier destruction and Lagrangian predictabilty at depth in a meandering jet*, Dyn. Atmos. Oceans **35** (2001), 41–61.

[47] ———, *Cross-jet Lagrangian transport and mixing in a $2\frac{1}{2}$ layer model*, J. Phys. Oceanogr. **34** (2004), no. 9, 1991–2005.